Ore Geology Reviews 57 (2014) 539–559

Contents lists available at ScienceDirect

Ore Geology Reviews

journal homepage: www.elsevier.com/locate/oregeorev

The formation of P-rich Fe–Ti oxide ore layers in the Taihe layered intrusion, SW China: Implications for magma-plumbing system process

Yu-Wei She [a,b], Song-Yue Yu [a], Xie-Yan Song [a,*], Lie-Meng Chen [a], Wen-Qin Zheng [a], Yan Luan [a,b]

[a] State Key Laboratory of Ore Deposit Geochemistry, Institute of Geochemistry, Chinese Academy of Sciences, Guiyang 550002, China
[b] Graduate University of Chinese Academy of Sciences, Beijing 100049, China

ARTICLE INFO

Article history:
Received 30 April 2013
Received in revised form 21 July 2013
Accepted 22 July 2013
Available online 1 August 2013

Keywords:
Taihe layered intrusion
Fe–Ti–P enriched magma
Phosphorus saturation
Early crystallization of Fe–Ti oxides
Magma-plumbing system

ABSTRACT

The Taihe intrusion is one of the layered intrusions that host giant Fe–Ti oxide deposit in the central part of the Emeishan Large Igneous Province, SW China. Different from the other layered intrusions, the Taihe intrusion has a massive Fe–Ti oxide ore layer at the top of the Lower Zone (LZ), particularly, the rocks of both Middle and Upper Zones contain as much as 5–12% apatite, and the most important Fe–Ti oxide ore layers (apatite magnetite clinopyroxenite) occur at the bases of cyclic units in the Middle Zone (MZ), rather than in the Lower Zone (LZ). High Cr and Ni concentrations of clinopyroxene (65–263 ppm and 66–83 ppm, respectively) and high An contents of plagioclase (79–80) of the LZ rocks indicate their more primitive parental magmas. The clinopyroxene and plagioclase of the MZ rocks are characterized by low Cr and Ni contents (1–21 ppm and 0.4–10 ppm, respectively) and low An (51–67), indicating more evolved parental magma. The Fe–Ti oxide ore layers in the MZ are not only high in Fe and Ti, but also enriched in P_2O_5 and rare earth elements, indicating an unusual Fe–Ti–P-rich parental magma. It is speculated that the MZ represents a later intrusion of Fe–Ti–P-rich magmas that were produced by the Fe–Ti enriched magma from a deep-seated magma chamber mixing with the extensively evolved P-rich magma in a middle level magma chamber. Early crystallization and cumulation of Fe–Ti oxide and apatite together with clinopyroxene from the Fe–Ti–P-rich magmas from the middle level magma chamber resulted in the formation of Fe–Ti oxide ore layers in the MZ. Fe–Ti–P-rich magma and apatite magnetite clinopyroxenites occur in the base of cyclic units, whereas apatite gabbros are presented at the upper parts of each cyclic unit. The Upper Zone (UZ) is the product of the crystallization of highly differentiated magma, consists chiefly of apatite gabbro and minor intercalated apatite clinopyroxenite.

1. Introduction

Accumulation of Fe–Ti oxides in layered intrusions has been attributed to sorting and settling of Fe–Ti oxide crystals from the evolved mafic magma (e.g. Tegner et al., 2006; Tollari et al., 2008; Wager and Brown, 1968). Thus, the Fe–Ti oxide layers commonly occur in the upper part of large layered intrusions, such as the Skearggard intrusion of East Greenland and Bushveld Complex of South Africa (Wager and Brown, 1968). However, they have also been found in the middle zone of the Sept Iles intrusion of Canada (Namur et al., 2010).

Several layered intrusions in central zone of the Emeishan Large Igneous Province (ELIP), such as Panzhihua, Hongge, Baima and Taihe, host world-class Fe–Ti oxide ore deposits (Panxi Geological Unit, 1984). These mafic–ultramafic intrusions are believed to be genetically linked with a Permian mantle plume (Chung and Jahn, 1995; Zhou et al., 2002). Thick massive Fe–Ti oxide layers mainly occur in the lower zone of the Panzhihua, Baima and Taihe intrusions and middle zone of the Hongge intrusion (Panxi Geological Unit, 1984; Song et al., 2013; Zhang et al., 2012; Zhong et al., 2002; Zhou et al., 2005). The Fe–Ti oxide layers in the Panzhihua and Baima intrusions have been interpreted to be the crystallization and accumulation of Fe–Ti oxides from the Fe–Ti enriched magmas resulted from fractional crystallization of basaltic magma at depths (Pang et al., 2008; Song et al., 2013; Zhang et al., 2012). Ganino et al. (2008) and Bai et al. (2012) proposed that elevation of oxygen fugacity due to reaction between the basaltic magma and footwall limestone has contribution to the early crystallization of the Fe–Ti oxides in the Panzhihua and Hongge intrusion as well.

Different from the Panzhihua and Baima intrusions, in which apatite crystallizes very late and is only concentrated in the upper zone gabbros, in the Taihe intrusion, thick magnetite clinopyroxenite layers containing as much as 5–12 modal% apatite occur in middle zone. This implies that the middle zone of the Taihe intrusion has an unusual genetic mechanism. Although Hou et al. (2012a) proposed that the Fe–Ti oxide ore layers of the Taihe intrusion were formed by crystallization of Fe–Ti oxide from a dense Fe–Ti-enriched magma, why the middle zone magnetite clinopyroxenites are so much rich in apatite has not been well understood.

* Corresponding author at: State Key Laboratory of Ore Deposit Geochemistry, Institute of Geochemistry, Chinese Academy of Sciences, 46th Guanshui Road, Guiyang 550002, China. Tel.: +86 851 5895538; fax: +86 851 5891664.
E-mail address: songxieyan@vip.gyig.ac.cn (X.-Y. Song).

0169-1368/$ – see front matter © 2013 Published by Elsevier B.V.
http://dx.doi.org/10.1016/j.oregeorev.2013.07.007

In this paper, more detailed studies of petrology and trace element and Sr–Nd isotope geochemistry of whole rock and mineral permit us to propose that the Taihe intrusion was formed in a complex magma plumbing system. We believe that the Lower Zone of the Taihe intrusion was crystallized from a differentiated magma from a deep-seated magma chamber. Whereas the later replenishing magmas are enriched in Fe, Ti as well as P due to magma-mixing and selected melting of fusible minerals, such as Fe–Ti oxides and apatite, in a middle level magma chamber. Apatite crystallized early together with the Fe–Ti oxides from such Fe–Ti–P enriched magma and formed the apatite magnetite clinopyroxenite layers in the Middle Zone of the Taihe intrusion.

2. Geological background

The ELIP composes of the Emeishan continental flood basalts covering an area of at least 5×10^5 km^2 and is genetically related to mafic–ultramafic intrusions and felsic plutons in the southwest China (Ali et al., 2005; Chung and Jahn, 1995; Song et al., 2001, 2004; Xu et al., 2001). The U–Pb age of the zircons separated from the mafic–ultramafic and felsic intrusions and the Emeishan basalts suggest an age of ~260 Ma for the ELIP magmatism (He et al., 2007; Zhong and Zhu, 2006; Zhong et al., 2011; Zhou et al., 2002, 2005, 2008). According to the ratio of Ti/Y, the Emeishan flood basalts have been defined as high-Ti and low-Ti series (Xiao et al., 2004; Xu et al., 2001), which were considered to have different origins, although this is subject to debate (Hou et al., 2011a; Shellnutt and Jahn, 2011).

In the central ELIP, the layered intrusions (Panzhihua, Xinjie, Hongge, Baima and Taihe) hosting giant Fe–Ti oxide deposits are situated along several N–S trending faults (Fig. 1). They can be subdivided into gabbro intrusions (e.g. Panzhihua and Baima) and clinopyroxenite-gabbro intrusions (e.g. Xinjie, Hongge and Taihe) based on different rock assemblage (Panxi Geological Unit, 1984). These intrusions are emplaced in the

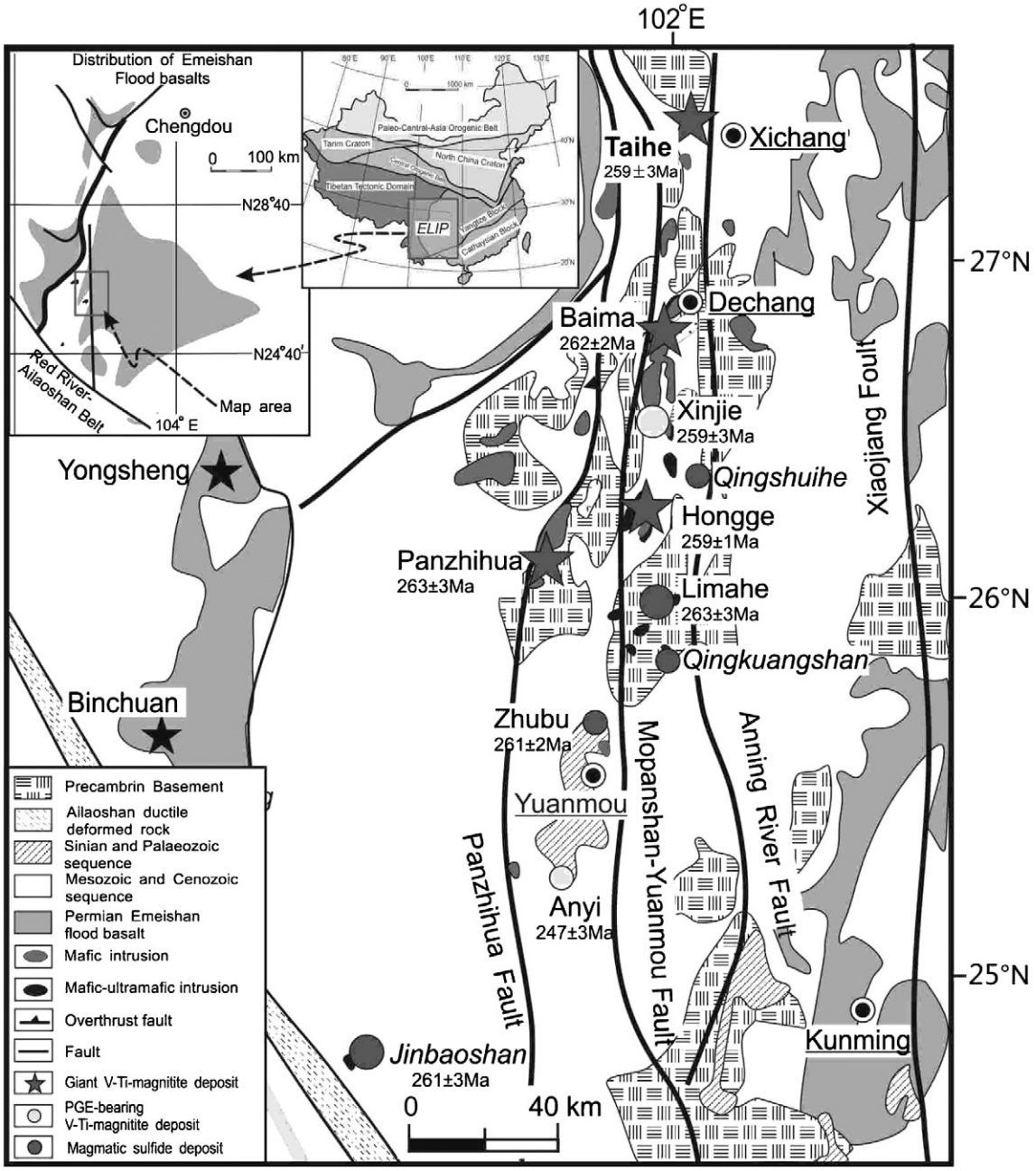

Fig. 1. Regional geological map of the central ELIP and locations of the mafic–ultramafic intrusions hosting Fe–Ti oxide deposit and magmatic sulfide deposit. Adapted from Song et al. (2009).

Proterozoic metasandstone, schists, and dolomitic limestone and/or intruded and surrounded by slightly later contemporaneous felsic rocks. These layered intrusions are believed to be related to the evolution of the high-Ti basaltic or picritic magmas, whereas, the contemporaneous small magmatic sulfide mineralized ultramafic intrusions, including Limahe and Jinbaoshan are related to low-Ti basaltic magmas (Fig. 1) (Zhou et al., 2008).

3. Petrography

The Taihe intrusion is a relatively small layered intrusion in the central ELIP and lies between the Mopanshan–Yuanmou and the Anninghe faults (Fig. 1) and dips to southeast with angles of 50–60° (Fig. 2b). The Taihe intrusion outcrops ~3 km long and 2 km wide, and extends more than 3 km southeastward underground and has a thickness of ~1.2 km. Although the Taihe intrusion is expected to be originally emplaced in the Neoproterozoic strata, like the other layered intrusions in the central ELIP, it is completely surrounded by a contemporaneous syenite pluton (261 ± 2 Ma, Xu et al., 2008) (Fig. 2a). The syenite dykes with thicknesses of several meters within the Taihe intrusion indicate that the syenite formed slightly later. On basis of the mineral assemblages and petrography textures of the samples from the drill hole ZK1707 (Fig. 3), the Taihe intrusion can be divided into three lithologic zones: lower zone (LZ), middle zone (MZ) and upper zone (UZ).

The ~200 m thick LZ comprises olivine clinopyroxenite, (olivine) gabbro and massive Fe–Ti oxide ore from the base to the top. The olivine clinopyroxenite contains 60–80 modal% clinopyroxene and 0–30% olivine, and minor plagioclase (7%) and Fe–Ti oxides (6%), as well as interstitial hornblende (2%). The (olivine) gabbro consists of 30–45% clinopyroxene, 45–60% plagioclase, up to 8% olivine, and 5–15% oxides and 1–3% hornblende. Olivine and minor lath-shaped plagioclase crystals can be enclosed by coarse-grained clinopyroxene in the clinopyroxenite and gabbro (Fig. 4a). The clinopyroxene usually displays exsolution oxide lamellae parallel to its prismatic cleavages. Opaque minerals (magnetite, ilmenite and traces of sulfides) occupy the interstitial regions between the silicates. The massive Fe–Ti oxide ores contain 40–70% magnetite, 15–40% ilmenite, <30% silicate minerals (including clinopyroxene, plagioclase and traces of interstitial hornblende), and up to 5% sulfides. Some subhedral–euhedral Fe–Ti oxides are enclosed in the clinopyroxene (Fig. 4b).

The ~500 m thick MZ is remarkable by abundance of apatite and consists of magnetite clinopyroxenites, apatite magnetite clinopyroxenites and (apatite) gabbro. Six rhythmic cycles are recognized in the MZ according to the variable mineral proportions (Fig. 3). The apatite magnetite clinopyroxenites comprising the lower half of the Cycles II, III, IV and V and VI generally contain 40–70% clinopyroxene, 5–15% magnetite, 5–20% ilmenite, 5–12% apatite, <10% plagioclase, <8% hornblende (locally up to ~20%), and variable contents of olivine. When the apatite magnetite clinopyroxenites contain more than 8% olivine, it is named as olivine apatite magnetite clinopyroxenites (Fig. 3). The euhedral apatite crystals occur together with anhedral magnetite and ilmenite (Fig. 4c–d). The (apatite) gabbros at the upper part of each cyclic unit contain 30–50% plagioclase, 30–40% clinopyroxene, 5–10% Fe–Ti oxides (locally up to 15%), <8% apatite and 1–6% hornblende. The magnetite clinopyroxenites with minor interstitial apatite that only occur in the Cycle I comprised ~10% magnetite, 8% ilmenite, 70–80% clinopyroxene, and up to 10% plagioclase.

The dominant rock type in the UZ is apatite gabbro, and a thin interlayer apatite clinopyroxenite occur in the lower part. This zone is marked by the appearance of large proportions of plagioclase and decrease of cumulus apatite content relative to the MZ. The apatite gabbro is composed of 50–75% plagioclase, 15–35% clinopyroxene, 5–10% Fe–Ti oxides, 5–8% apatite and minor interstitial hornblende (3–10%). The plagioclase occurs as oriented subhedral to euhedral tabular crystals.

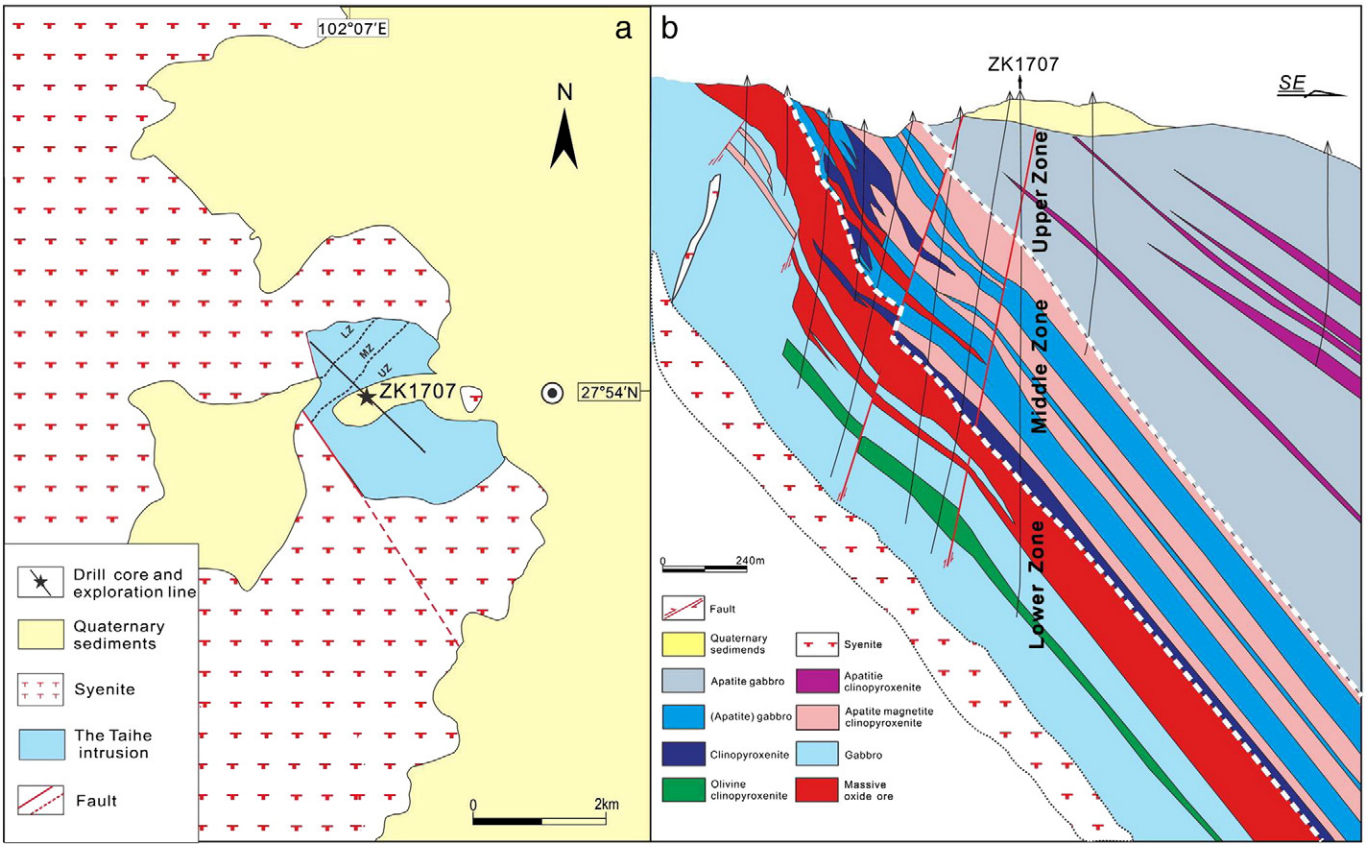

Fig. 2. (a) Simplified geological map of the Taihe layered intrusion. The drill-core of ZK 1707 is indicated and samples were collected. (b) Cross sections of exploration line 17 from the Taihe intrusion.

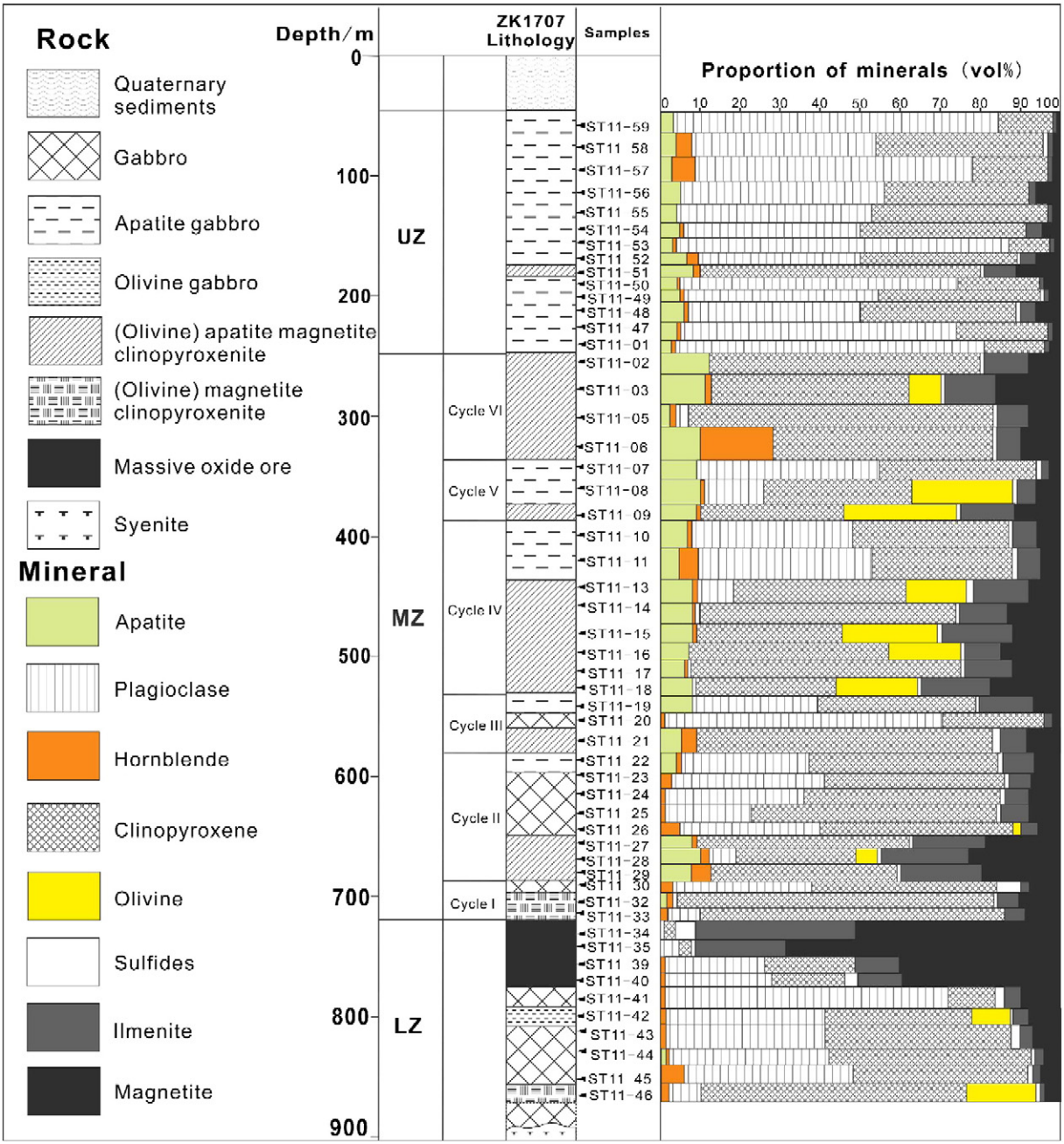

Fig. 3. Stratigraphic column of the Taihe intrusion shows the general petrographic variations and the proportion of minerals. UZ is the Upper Zone; MZ is the Middle Zone; and LZ is the Lower Zone.

Euhedral apatite occurs as cumulus phase. The hornblende and Fe–Ti oxides occur as intercumulus between the plagioclase.

4. Sampling and analytical methods

In this study, 53 samples were collected from exploration bore hole (ZK1707), which cut through three lithologic zones in the Taihe intrusion (Fig. 2b). Two apatite gabbro samples for geochronology analysis of the Taihe intrusion are collected from the open-pit mine, where the UZ gabbro is very well exposed due to extensive mining.

Zircon grains were separated using conventional heavy liquid and magnetic techniques, and then handpicked out under binocular microscope to select zircon grains for analysis. The individual zircon crystals were mounted in epoxy, and then polished for cathodoluminescence (CL) observation prior to U–Pb isotopic analyses. The U–Pb isotopic ratios of zircons were measured using the SHRIMP II at the Chinese Academy of Geological Sciences, Beijing, China. The standard TEM zircons (417 Ma, with variable U-content, Black et al., 2003) were used to monitor inter-element fractionation, and U, Th and Pb concentrations were determined based on the standard zircons M257 (561.3 Ma, U = 840 ppm, Nasdala et al., 2008). Uncertainties for each analysis are at 1σ, whereas the weighted mean age is quoted at 2σ. Zircon U–Pb data are listed in Table 1.

Major elements were obtained by X-ray fluorescence spectrometer (XRF) at the ALS Laboratory Group, Guangzhou, using fused lithium-tetraborate glass pellets. The ferric and ferrous iron were determined by wet chemical method. The analytical precision as determined on the Chinese National standard GSR-3 was generally around 1–5%. Trace elements were analyzed by inductively coupled plasma mass spectrometry (ICP-MS) using the technique of Qi et al. (2000) at the Institute of Geochemistry, Chinese Academy of Sciences (IGCAS). The international standards GBPG-1, OU-6, and the Chinese national

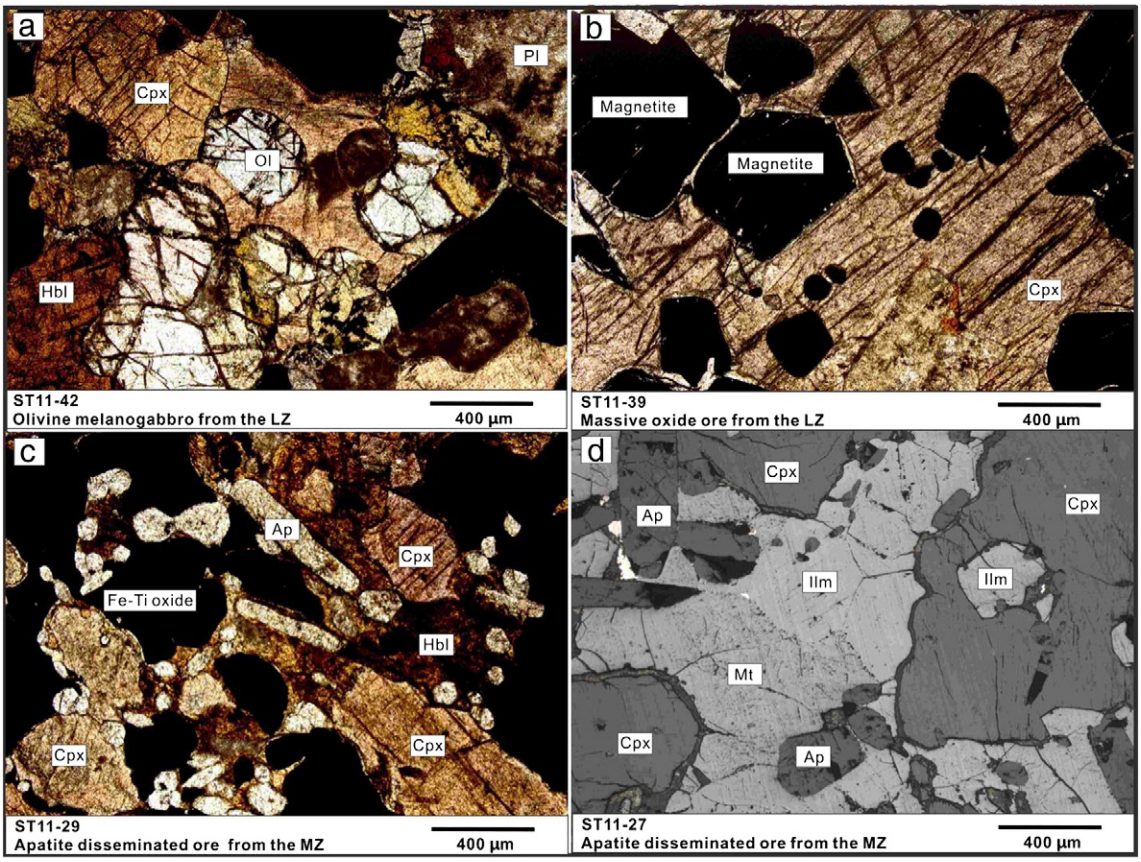

Fig. 4. Microscope photos under plant-polarized light and reflected light showing rock textures of the Taihe intrusion. (a) Rounded olivine enclosed in clinopyroxene in the LZ olivine gabbro; (b) Early crystallized subhedral–euhedral magnetite enclosed in clinopyroxene of the LZ massive ore; (c) subhedral–euhedral hexagonal prismatic apatite coexisting with Fe–Ti oxide and silicates in the MZ apatite magnetite clinopyroxenite; (d) Abundant apatite and high proportional ratio between ilmenite and magnetite in the MZ apatite magnetite clinopyroxenite. Ol = Olivine; Cpx = Clinopyroxene; Pl = Plagioclase; Ap = Apatite; Hbl = Hornblende; Mt = Magnetite; Ilm = Ilmenite.

Table 1
SHRIMP zircon analytical data for the Taihe intrusion.

Spot	U (ppm)	Th (ppm)	$^{206}Pb_c$ (%)	$^{206}Pb^*$ (ppm)	$^{232}Th/^{238}U$	(1) $^{206}Pb/^{238}U$ (age)	(2) $^{206}Pb/^{238}U$ (age)	(3) $^{206}Pb/^{238}U$ (age)
ST11-A1								
ST11-A1-1	607	111	0.58	22	0.19	264.2 ± 5.1	264.7 ± 5.1	265.1 ± 5.3
ST11-A1-2	208	151	0.71	7.63	0.75	267.9 ± 5.4	267.1 ± 5.4	267.0 ± 6.2
ST11-A1-3	168	158	2.01	6.17	0.97	264.9 ± 5.5	266.0 ± 5.5	265.6 ± 6.8
ST11-A1-4	1138	542	0.58	40	0.49	257.3 ± 4.9	257.4 ± 5.0	257.8 ± 5.4
ST11-A1-5	229	321	1.73	8.48	1.45	267.5 ± 5.6	267.3 ± 5.6	267.4 ± 7.5
ST11-A1-6	1464	1011	0.32	53	0.71	265.4 ± 5.0	265.7 ± 5.1	266.8 ± 5.7
ST11-A1-7	549	345	0.31	19	0.65	253.7 ± 4.9	253.5 ± 4.9	254.2 ± 5.5
ST11-A1-8	615	402	0.70	21.4	0.68	254.0 ± 5.1	254.5 ± 5.1	255.8 ± 5.7
ST11-A1-9	442	135	0.47	16.3	0.32	269.5 ± 5.2	269.8 ± 5.3	269.7 ± 5.5
ST11-A1-10	4838	112	0.09	175	0.02	265.8 ± 5.0	266.0 ± 5.0	265.9 ± 5.0
ST11-A1-11	622	244	0.28	21.2	0.41	249.5 ± 4.8	249.6 ± 4.8	250.0 ± 5.2
ST11-A1-12	478	231	0.45	16.8	0.50	257.2 ± 5.0	257.5 ± 5.0	257.7 ± 5.4
ST11-A1-13	456	703	0.36	15.9	1.59	255.3 ± 5.9	255.9 ± 5.9	257.6 ± 8.0
ST11-A1-14	584	339	0.35	20.2	0.60	253.5 ± 5.0	253.8 ± 5.0	255.0 ± 5.5
ST11-A1-15	503	946	0.25	17.1	1.94	250.3 ± 4.9	250.4 ± 4.9	253.1 ± 7.2
ST11-A1-16	87	33	2.71	3.12	0.39	255.7 ± 5.9	255.9 ± 5.6	257.7 ± 6.0
ST11-A2								
ST11-A2-1	171	136	0.86	6.09	0.82	259.8 ± 5.3	259.2 ± 5.3	258.8 ± 6.2
ST11-A2-2	246	330	0.46	8.85	1.39	263.2 ± 5.3	263.6 ± 5.3	265.3 ± 6.9
ST11-A2-3	392	664	0.76	13.8	1.75	257.4 ± 5.3	257.8 ± 5.3	263.4 ± 7.6
ST11-A2-4	467	884	0.54	16.1	1.96	253.1 ± 5.3	253.4 ± 5.3	254.9 ± 7.9
ST11-A2-5	319	450	1.06	11.4	1.46	259.6 ± 5.2	259.0 ± 5.2	261.6 ± 6.9
ST11-A2-6	343	430	1.22	11.9	1.30	251.4 ± 5.0	251.5 ± 5.0	252.9 ± 6.4
ST11-A2-7	315	402	0.95	10.9	1.32	252.4 ± 5.2	252.6 ± 5.1	255.0 ± 6.6

Errors are 1-sigma; Pb_c and Pb^* indicate the common and radiogenic portions, respectively.
Error in standard calibration was 0.64% (not included in above errors but required when comparing data from different mounts).
(1) Common Pb corrected using measured ^{204}Pb.
(2) Common Pb corrected by assuming $^{206}Pb/^{238}U$–$^{207}Pb/^{235}U$ age-concordance.
(3) Common Pb corrected by assuming $^{206}Pb/^{238}U$–$^{208}Pb/^{232}Th$ age-concordance.

Table 2
Major and trace element compositions of the rocks of the Taihe intrusion.

Sample	ST11-59	ST11-58	ST11-57	ST11-56	ST11-55	ST11-54	ST11-53	ST11-52	ST11-51	ST11-50	ST11-49	ST11-48	ST11-47
Depth (m)	63	81	98	113	130	146	154	169	173	185	198	216	226
Rock	Ap Gab	Ap Gab	Ap Gab	Ap Gab	Ap Gab	Ap Gab	Ap Gab	Ap Gab	Ap Mt Cpx	Ap Gab	Ap Gab	Ap Gab	Ap Gab
Zone	UZ	UZ	UZ	UZ	UZ	UZ	UZ	UZ	UZ	UZ	UZ	UZ	UZ
Cyclic unit													
Major elements (wt.%)													
SiO_2	45.7	42.1	43.6	41.4	43.9	41.3	45.4	33.0	28.0	43.1	43.3	37.0	41.1
TiO_2	1.99	2.84	2.11	3.44	2.14	3.32	2.65	5.15	6.7	2.19	2.93	3.57	2.17
Al_2O_3	22.1	19.1	20.8	18.7	18.4	20.3	23.2	12.3	6.9	21.3	21.0	17.2	20.9
Fe_2O_3(t)	8.4	11.0	9.6	10.7	10.6	9.2	4.8	20.0	27.7	8.3	8.7	14.0	8.2
MnO	0.12	0.13	0.10	0.18	0.20	0.13	0.09	0.24	0.33	0.11	0.15	0.17	0.10
MgO	3.13	3.80	2.86	4.82	3.86	4.28	2.48	6.42	8.00	2.72	3.76	4.64	3.32
CaO	7.9	11.6	13.1	10.6	10.3	12.8	13.1	15.0	17.2	12.4	10.6	14.5	14.4
Na_2O	4.05	3.13	3.29	3.32	3.77	2.90	3.46	1.19	0.44	3.16	3.12	1.50	2.22
K_2O	1.41	0.76	0.34	0.94	1.11	0.42	0.65	0.63	0.05	1.08	2.06	1.38	1.45
P_2O_5	1.10	1.59	1.34	1.93	1.61	2.01	1.00	2.37	3.30	1.39	1.69	2.02	1.58
LOI	3.13	2.85	1.50	2.97	2.13	1.68	2.53	1.99	0.81	3.79	2.43	2.08	2.93
Total	99.0	99.0	98.6	99.0	98.0	98.4	99.4	98.2	99.5	99.5	99.7	98.1	98.3
FeO	5.49	6.77	5.62	7.48	7.08	6.20	3.69	10.65	14.00	4.84	6.00	8.29	5.09
Fe_2O_3	2.31	3.52	3.36	2.41	2.76	2.30	0.74	8.16	12.12	2.93	1.98	4.82	2.55
Fe^{3+}/Ti^{4+}	1.16	1.24	1.59	0.70	1.29	0.69	0.28	1.59	1.81	1.34	0.68	1.35	1.18
Trace elements (ppm)													
Sc	4.5	11.8	8.0	7.9	5.6	5.5	5.8	17.4	22.2	7.1	5.6	14.3	9.7
V	198	307	270	225	214	200	105	456	605	201	191	387	213
Cr	1.22	1.17	1.23	1.01	1.84	1.25	1.31	3.71	5.48	1.25	1.11	1.89	3.22
Co	33.0	44.2	47.2	47.2	47.3	48.0	30.4	67.8	87.6	31.3	35.5	47.7	35.5
Ni	6.19	10.11	14.31	1.31	5.84	1.18	2.95	8.63	9.97	2.34	1.47	2.87	2.24
Cu	16.5	87.3	53.2	64.6	36.9	50.8	15.9	69.2	88.0	25.9	19.8	44.9	19.7
Ga	16.1	17.9	18.2	17.2	19.8	16.9	16.6	18.1	18.8	17.3	17.0	18.2	17.4
Rb	62.3	33.3	9.6	40.4	40.4	14.3	19.5	24.0	1.9	46.9	86.5	52.1	62.0
Sr	1890	1810	2090	1720	1700	2550	2930	1420	743	2400	2040	2000	2500
Y	12.6	16.4	15.3	18.6	29.1	17.2	14.9	25.6	36.8	16.6	16.3	20.0	15.4
Zr	20.4	19.0	12.4	20.0	238.0	18.6	23.7	21.6	36.3	20.0	19.0	17.3	14.9
Nb	4.80	3.73	3.93	6.87	26.40	6.59	9.68	3.83	4.95	3.95	6.65	2.90	2.70
Ba	478	276	236	402	314	297	386	251	54	482	675	344	349
La	15.7	18.5	16.4	22.1	57.4	22.3	15.9	27.7	36.6	21.6	21.2	18.1	17.1
Ce	38.6	46.4	39.8	54.6	115.0	55.2	33.6	67.9	91.2	51.6	49.7	47.4	42.7
Pr	5.63	6.97	6.13	8.28	14.80	8.20	5.39	11.50	15.50	7.70	7.61	7.79	6.67
Nd	28.4	35.6	30.7	41.9	61.8	40.9	26.9	57.9	79.3	37.2	37.0	41.9	34.6
Sm	6.15	8.03	6.98	8.99	12.10	8.86	5.90	13.00	17.80	8.10	7.77	9.61	7.78
Eu	2.62	3.16	3.25	3.60	3.79	3.72	3.05	4.87	6.26	3.60	3.44	3.88	3.41
Gd	5.28	6.97	6.65	8.11	10.27	7.85	5.38	12.48	17.08	6.98	6.96	8.64	6.89
Tb	0.65	0.89	0.84	1.00	1.39	0.97	0.72	1.56	2.10	0.90	0.87	1.09	0.85
Dy	2.92	3.86	3.54	4.18	6.22	4.00	3.18	6.63	9.23	3.87	3.75	4.64	3.68
Ho	0.53	0.68	0.69	0.73	1.14	0.71	0.59	1.20	1.69	0.69	0.63	0.81	0.64
Er	1.18	1.48	1.50	1.66	2.74	1.54	1.40	2.60	3.62	1.55	1.40	1.73	1.37
Tm	0.12	0.15	0.15	0.16	0.32	0.15	0.14	0.27	0.36	0.15	0.15	0.18	0.14
Yb	0.68	0.84	0.83	0.89	1.96	0.89	0.85	1.45	2.05	0.86	0.82	0.89	0.70
Lu	0.09	0.11	0.12	0.12	0.27	0.11	0.11	0.18	0.27	0.11	0.10	0.12	0.09
Hf	0.50	0.59	0.47	0.60	4.52	0.48	0.64	0.93	1.38	0.59	0.54	0.63	0.49
Ta	0.29	0.23	0.17	0.45	1.13	0.45	0.50	0.29	0.39	0.26	0.40	0.20	0.20
Th	0.40	0.48	0.39	0.45	4.05	0.43	0.61	0.43	0.61	0.42	0.53	0.24	0.29
U	0.16	0.11	0.28	0.12	0.71	0.14	0.24	0.15	0.18	0.11	0.28	0.07	0.10

Ap = Apatite; Gab = Gabbro; Mt = Magnetite; Cpx = Clinopyroxene; Ol = Olivine; Ore = Oxide ore.
UZ = Upper Zone; MZ = Middle Zone; LZ = Lower Zone.

standard GSR-3 were used for analytical quality control, with the precision generally better than 5%. Major oxide and trace element analyses of the samples are listed in Table 2.

The major elements of olivine and plagioclase in this study were determined by wavelength dispersive X-ray analysis using an EPMA-1600 electron microprobe at the Institute of Geochemistry, Chinese Academy of Science (IGCAS). Accelerating voltage is 25 kV and a beam current of 10 nA was used. The accuracy of analysis was monitored using mineral standards: pyrope for Mg, Al, Cr and Mn, rutile for Ti, magnetite for Fe and olivine for Ni. The detection limits for these elements are 0.01%, and errors are within 2%. The average compositions of olivine and plagioclase in each sample are listed in Tables 3 and 4.

The major oxides and trace elements of clinopyroxene were determined by the LA-ICP-MS apparatus using the method of Liu et al. (2008) at the Institute of Geochemistry, Chinese Academy of Sciences. The international standards NIST SRM 610, BCR-2G, BIR-1G and BHVO-2G (from USGS) are used as external calibration for the clinopyroxene in situ analysis. Measured values of reference glasses agree well with the recommended values of these standards, and precision is higher than 5% for most of the elements. The average compositions of clinopyroxene in each sample are listed in Table 5.

For whole-rock Sr–Nd isotopic analyses were carried out using the MC-ICP-MS at the Guangzhou Institute of Geochemistry, Chinese

ST11-01	ST11-02	ST11-03	ST11-05	ST11-06	ST11-07	ST11-08	ST11-09	ST11-10	ST11-11	ST11-13	ST11-14	ST11-15	ST11-16
236	246	270	305	323	342	363	381	400	415	443	459	471	490
Ap Gab	Ap Mt Cpx	Ap Mt Cpx	Mt Cpx	Ap Mt Cpx	Ap Gab	Ap Gab	Ap Mt Cpx	Ap Gab	Ap Gab	Ap Mt Cpx	Ap Mt Cpx	Ap Mt Cpx	Ap Mt Cpx
UZ	MZ	MZ	MZ	MZ	MZ	MZ	MZ	MZ	MZ	MZ	MZ	MZ	MZ
	VI	VI	VI	VI	V	V	V	IV	IV	IV	IV	IV	IV
45.9	24.8	21.2	32.7	25.9	30.2	31.0	25.0	34.3	34.0	27.3	27.0	22.7	25.2
1.7	9.5	10.03	6.61	7.9	5.53	7.39	10.04	6.9	5.09	9.17	9.39	11.95	10.25
24.7	4.3	3.0	6.0	6.5	7.6	7.8	2.8	12.9	13.3	4.7	3.9	2.9	3.5
4.4	27.4	31.9	24.4	25.8	18.7	22.9	32.0	20.1	20.8	29.5	30.8	35.4	32.8
0.07	0.35	0.40	0.32	0.36	0.26	0.31	0.39	0.22	0.20	0.38	0.37	0.42	0.41
2.09	11.87	12.55	10.32	10.34	8.18	10.73	12.79	5.75	5.38	10.49	11.65	11.97	12.01
11.7	14.9	13.2	15.8	16.0	22.1	14.3	12.6	14.2	13.2	13.2	13.8	11.6	12.5
3.56	0.39	0.29	0.71	0.74	0.59	1.05	0.30	1.68	1.56	0.58	0.43	0.28	0.35
1.28	0.05	0.02	0.22	0.18	0.09	0.15	0.02	0.46	0.57	0.19	0.04	0.02	0.04
0.93	4.87	4.47	0.54	3.85	3.45	3.98	3.28	2.62	1.62	3.14	3.02	2.95	2.81
3.29	1.37	2.97	1.05	1.35	2.54	0.22	0.67	0.55	3.62	0.21	0.00	0.00	0.00
99.6	99.8	99.9	98.7	98.9	99.3	99.9	99.8	99.8	99.3	98.7	100.0	99.7	99.6
3.33	14.35	14.20	12.20	14.40	8.49	14.60	18.00	11.45	13.05	18.25	18.60	20.80	19.10
0.74	11.47	16.09	10.82	9.84	9.29	6.72	11.96	7.42	6.28	9.21	10.15	12.26	11.53
0.44	1.21	1.60	1.64	1.25	1.68	0.91	1.19	1.07	1.23	1.00	1.08	1.03	1.13
1.4	18.6	22.9	29.5	19.6	16.4	21.0	29.0	20.7	16.1	28.2	30.0	26.0	29.2
86	618	613	625	515	404	423	692	531	436	629	730	731	755
1.23	7.67	12.30	17.90	9.68	29.00	7.75	10.60	3.75	11.60	6.19	6.31	31.50	8.51
34.9	109.0	140.0	74.1	93.6	58.6	80.8	116.0	92.1	118.0	94.8	104.0	117.0	121.0
1.39	2.12	2.61	160.14	2.62	5.42	1.95	2.02	2.33	14.99	3.51	3.58	17.04	3.52
8.9	102.0	133.0	174.0	83.0	58.2	66.9	112.0	91.8	161.0	120.0	107.0	139.0	155.0
16.3	16.1	13.3	16.5	15.5	14.7	13.3	14.9	17.8	19.1	15.6	16.1	15.2	15.2
56.4	1.5	0.7	4.2	7.7	1.6	4.0	0.5	10.3	15.8	9.2	1.2	0.4	0.8
2510	609	476	310	904	961	901	244	1230	1010	419	316	216	275
7.9	40.9	30.7	26.6	38.7	39.3	31.8	33.1	24.4	18.2	37.1	29.7	28.7	29.7
11.9	37.0	26.8	45.0	30.4	62.0	17.2	26.1	20.2	16.7	44.5	23.0	23.9	24.0
3.86	10.50	7.11	5.44	7.78	4.02	6.62	8.62	6.71	5.69	10.40	6.51	8.55	7.26
345	28	26	146	215	42	56	14	145	199	48	19	10	14
13.7	45.1	29.4	13.0	43.4	41.3	29.2	26.5	22.6	16.6	31.9	21.6	23.6	22.7
30.2	114.0	77.5	38.5	104.0	98.3	80.9	73.4	61.0	43.4	84.7	59.7	61.9	60.0
4.36	17.80	13.60	6.95	17.00	16.00	14.20	12.90	10.30	7.13	14.40	10.80	11.10	11.00
21.2	88.7	69.3	37.5	81.6	79.7	74.0	67.1	52.8	35.7	75.8	58.2	58.1	58.4
4.22	19.40	15.60	9.65	17.80	17.60	16.80	15.30	11.70	8.29	17.60	14.00	13.30	13.60
2.49	6.51	5.71	3.61	6.31	6.10	5.67	5.07	4.20	3.43	5.51	4.71	4.43	4.60
3.67	17.25	14.26	9.36	15.73	16.13	14.81	14.66	10.52	7.66	17.15	14.12	13.71	14.22
0.45	2.12	1.81	1.29	2.01	2.07	1.88	1.86	1.39	0.99	2.09	1.71	1.62	1.69
1.85	9.09	7.37	6.01	8.64	8.96	7.71	7.88	5.94	4.31	9.05	7.11	6.88	7.06
0.32	1.58	1.29	1.14	1.55	1.63	1.34	1.40	1.05	0.80	1.55	1.29	1.24	1.29
0.70	3.50	2.83	2.49	3.50	3.62	2.91	3.08	2.31	1.72	3.36	2.80	2.65	2.66
0.07	0.34	0.25	0.27	0.34	0.36	0.26	0.30	0.21	0.16	0.34	0.26	0.24	0.25
0.40	1.89	1.34	1.49	1.89	2.01	1.40	1.59	1.13	0.88	1.79	1.45	1.36	1.44
0.05	0.23	0.18	0.22	0.25	0.29	0.18	0.20	0.15	0.12	0.24	0.19	0.19	0.20
0.36	1.19	1.07	1.57	0.95	1.64	0.73	1.03	0.76	0.61	1.52	0.96	0.91	0.91
0.29	0.79	0.70	0.37	0.51	0.38	0.61	0.70	0.51	0.35	0.75	0.51	0.77	0.65
0.28	0.67	0.21	0.31	0.63	0.81	0.32	0.35	0.31	0.22	0.90	0.33	0.28	0.28
0.09	0.16	0.04	0.12	0.21	0.21	0.08	0.10	0.08	0.09	0.22	0.08	0.06	0.07

(*continued on next page*)

Academy of Sciences. The analytical errors are less than 0.005% for $^{87}Sr/^{86}Sr$ and $^{143}Nd/^{144}Nd$ ratios. Standard errors (2σm) for the Sr and Nd isotope analyses are listed in Table 6.

5. Analytical results

5.1. Zircon U–Pb age

Analyses of the sixteen individual zircon crystals from the ST11-A1 form a single age group and yield a mean $^{206}U/^{238}Pb$ age of 259 ± 3 Ma with a mean square of weighted deviations (MSWD) of 1.7 (Fig. 5a). This is supported by the data of the ST11-A2, which yields a mean $^{206}U/^{238}Pb$ age of 257 ± 4 Ma with a MSWD of 0.74 (Fig. 5b). The zircon age are consistent with the age (259 ± 2 Ma) reported by Zhong et al. (2011).

5.2. Whole rock chemical correlations

Similar to the Panzhihua intrusion, the Taihe rocks plot two distinct trends in the diagrams of $Fe_2O_3(t)$ and V against TiO_2 (Song et al., 2013). The LZ rocks of the Taihe and Panzhihua intrusions plot on the same trend showing relative high $Fe_2O_3(t)/TiO_2$ and V/TiO_2 ratios, whereas, the MZ rocks of the Taihe intrusion and the UZ rocks of the Panzhihua intrusion plot on the trend with relatively high $Fe_2O_3(t)/TiO_2$ and V/TiO_2

Table 2 (*continued*)

Sample	ST11-17	ST11-18	ST11-19	ST11-20	ST11-21	ST11-22	ST11-23	ST11-24	ST11-25	ST11-26	ST11-27	ST11-28	ST11-29
Depth (m)	506	517	534	558	575	589	602	616	629	641	653	665	677
Rock	Ap Mt Cpx	Ap Mt Cpx	Ap Gab	Gab	Ap Mt Cpx	Gab	Gab	Gab	Gab	Gab	Ap Mt Cpx	Ap Mt Cpx	Ap Mt Cpx
Zone	MZ	MZ	MZ	MZ	MZ	MZ	MZ	MZ	MZ	MZ	MZ	MZ	MZ
Cyclic unit	IV	IV	III	III	III	II	II	II	II	II	II	II	II
Major elements (wt.%)													
SiO_2	28.1	22.2	30.3	45.5	31.5	33.3	35.8	34.2	34.6	37.9	18.8	13.4	18.0
TiO_2	9.07	12.07	8.8	2.01	9.99	8.71	6.83	5.95	6.04	4.81	14.15	15.65	13.64
Al_2O_3	4.0	3.3	9.3	21.2	4.2	8.4	8.7	11.2	10.5	9.5	3.8	3.9	4.0
Fe_2O_3(t)	29.7	35.2	23.9	8.2	25.0	25.7	24.1	26.0	26.2	21.5	39.4	47.0	41.3
MnO	0.38	0.42	0.25	0.10	0.28	0.24	0.25	0.23	0.25	0.23	0.30	0.31	0.30
MgO	12.00	11.07	6.94	3.37	10.14	8.39	8.81	7.11	7.73	8.86	8.19	7.01	8.00
CaO	12.8	11.7	14.6	11.8	16.0	13.4	13.5	11.9	12.3	14.5	11.9	9.9	11.7
Na_2O	0.44	0.30	1.20	3.55	0.48	1.05	1.08	1.36	1.28	1.10	0.29	0.19	0.28
K_2O	0.08	0.02	0.43	0.98	0.08	0.32	0.23	0.32	0.37	0.59	0.03	0.01	0.03
P_2O_5	2.11	3.07	3.09	0.24	2.02	0.79	0.19	0.17	0.20	0.39	2.79	3.35	2.90
LOI	0.00	0.39	1.06	2.70	0.04	0.00	0.42	0.34	0.17	0.41	0.00	0.00	0.00
Total	98.6	99.7	99.8	99.7	99.7	99.7	99.9	98.7	99.6	99.8	99.2	99.4	99.8
FeO	18.40	19.75	13.30	5.49	15.20	14.40	13.60	14.75	14.70	12.15	23.10	25.20	22.80
Fe_2O_3	9.23	13.24	9.07	2.13	8.07	9.70	9.03	9.56	9.87	7.98	13.74	19.00	16.00
Fe^{3+}/Ti^{4+}	1.02	1.10	1.03	1.06	0.81	1.11	1.32	1.61	1.64	1.66	0.97	1.21	1.17
Trace elements (ppm)													
Sc	30.5	25.6	24.9	11.8	42.4	32.8	33.8	25.1	28.0	32.0	29.5	23.8	27.9
V	711	824	621	242	701	776	726	813	795	651	1150	1420	1200
Cr	6.33	8.69	4.80	10.40	6.23	8.03	6.00	12.30	15.70	27.20	17.00	21.10	14.80
Co	112.0	121.0	98.4	45.9	105.0	109.0	93.8	115.0	112.0	86.9	146.0	176.0	162.0
Ni	3.93	4.09	8.97	6.55	36.80	45.88	40.21	48.95	44.86	26.69	13.52	25.67	19.88
Cu	133.0	165.0	167.0	81.7	227.0	240.0	169.0	190.0	165.0	88.0	206.0	248.0	234.0
Ga	15.5	15.8	16.7	19.1	14.0	17.3	17.4	21.2	20.7	17.7	20.3	22.2	21.6
Rb	3.2	0.4	17.3	36.7	3.8	12.6	10.5	10.9	13.0	19.9	0.5	1.5	0.6
Sr	286	253	871	1940	333	627	550	885	789	726	200	195	201
Y	27.0	28.8	25.8	9.3	23.8	12.5	12.8	9.9	12.1	15.3	21.0	18.2	21.1
Zr	24.4	25.3	23.7	18.9	35.7	27.4	30.2	21.5	26.6	28.5	28.3	24.4	26.0
Nb	6.99	9.12	8.10	2.93	7.36	7.00	5.49	3.30	4.71	3.62	9.18	8.03	7.62
Ba	28	11	96	284	61	118	85	97	92	159	17	9	13
La	19.3	23.5	22.2	9.5	13.0	6.3	5.6	4.9	6.7	9.7	17.9	16.7	18.7
Ce	52.2	62.4	57.7	22.2	37.7	17.3	15.6	13.0	17.2	24.9	47.4	43.7	48.8
Pr	9.37	11.20	10.20	3.21	6.97	3.16	2.84	2.37	2.95	4.24	8.24	7.63	8.41
Nd	50.3	59.1	53.1	15.6	38.5	18.0	16.0	12.6	15.5	22.3	43.2	40.4	45.5
Sm	12.20	13.60	12.20	3.68	9.74	4.53	4.45	3.34	4.13	5.65	10.20	9.26	10.20
Eu	4.19	4.57	4.48	2.02	3.36	1.92	1.85	1.57	1.75	2.24	3.32	3.07	3.35
Gd	12.55	14.27	13.03	3.40	9.53	4.79	4.62	3.53	4.07	5.61	9.96	9.21	10.12
Tb	1.45	1.61	1.51	0.47	1.21	0.64	0.64	0.48	0.58	0.79	1.22	1.07	1.25
Dy	6.44	6.85	6.15	2.06	5.82	2.94	3.08	2.38	2.63	3.60	5.13	4.52	5.36
Ho	1.20	1.23	1.10	0.39	1.03	0.56	0.57	0.45	0.51	0.68	0.95	0.79	0.96
Er	2.50	2.64	2.46	0.88	2.22	1.19	1.29	0.98	1.15	1.53	1.95	1.77	2.07
Tm	0.25	0.25	0.24	0.11	0.23	0.13	0.15	0.12	0.14	0.16	0.20	0.16	0.19
Yb	1.41	1.35	1.25	0.57	1.28	0.72	0.81	0.64	0.78	0.91	1.02	0.87	1.06
Lu	0.18	0.19	0.17	0.07	0.18	0.10	0.11	0.08	0.10	0.12	0.13	0.12	0.14
Hf	1.06	0.89	0.92	0.58	1.39	1.07	1.18	0.85	1.08	1.16	1.14	1.01	1.06
Ta	0.61	0.81	0.63	0.21	0.64	0.50	0.37	0.24	0.29	0.24	0.75	0.67	0.62
Th	0.26	0.28	0.30	0.43	0.29	0.19	0.21	0.16	0.38	0.37	0.27	0.25	0.24
U	0.06	0.06	0.08	0.10	0.08	0.05	0.04	0.04	0.10	0.09	0.06	0.06	0.06

ratios (Fig. 6a–b). Although the Taihe LZ rocks show a similar positive correlation between P_2O_5 and SiO_2 with the LZ and MZ of the Panzhihua intrusion, most of the Taihe MZ and UZ samples display negative correlation similar to the Panzhihua UZ rocks (Fig. 6c). It is noteworthy that P_2O_5 contents (as P_2O_5 >1 wt.%) are positively correlated with Fe_2O_3(t) in the Taihe MZ and UZ rocks, comparable with the UZ rocks of the Panzhihua intrusion (Fig. 6e).

5.3. Chemostratigraphic variation

The LZ gabbro and olivine clinopyroxenite have low contents of Fe_2O_3(t) (13–21 wt.%), and high P_2O_5 (0.06–0.19 wt.%) and ratios of Fe^{3+}/Ti^{4+} (1.5–1.8) relative to the massive oxide ores, which contain 52–69 wt.% Fe_2O_3(t) and P_2O_5 (0.02–0.04 wt.%) and Fe^{3+}/Ti^{4+} ratios of 2.2–2.3 (except for the sample ST11-34) (Fig. 7a–c, Table 2). In the LZ rocks, olivine has small variation in forsterite percentage (Fo = ~71), anorthite contents of plagioclase (An) vary from 79 to 80, clinopyroxene has Mg# ranging from 76 to 79 and high Cr (65–263 ppm) and Ni (66–83 ppm). Whereas, clinopyroxenes in the massive ores have relatively low Cr (7–22 ppm) and Ni (58–73 ppm), and plagioclases have higher An (= 78–86).

For the MZ, the (apatite) magnetite clinopyroxenites in the lower half of each cyclic units commonly contain 24–47 wt.% Fe_2O_3(t) and 1.3–4.9 wt.% P_2O_5 (except for a few samples), and have Fe^{3+}/Ti^{4+} ratios ranging 0.8 to 1.6. The (apatite) gabbros comprising the upper half of each cyclic unit have low Fe_2O_3(t) contents (8–26 wt.%) and

ST11-30	ST11-32	ST11-33	ST11-34	ST11-35	ST11-39	ST11-40	ST11-41	ST11-42	ST11-43	ST11-44	ST11-45	ST11-46
688	698	714	728	744	756	765	780	804	820	839	854	871
Gab	Mt Cpx	Mt Cpx	Ore	Ore	Ore	Ore	Gab	Ol Gab	Gab	Gab	Gab	Ol Cpx
MZ	MZ	MZ	LZ	LZ	LZ	LZ	LZ	LZ	LZ	LZ	LZ	LZ
I	I	I										
37.8	30.8	30.7	0.9	0.6	13.4	13.4	37.8	37.4	36.2	41.2	38.5	41.2
4.62	7.86	11.11	21.3	16.85	11.8	11.3	3.32	3.89	4.85	3.32	3.38	2.81
12.3	5.8	4.7	4.4	4.6	12.1	12.5	23.0	15.0	10.3	12.2	15.3	9.7
21.5	29.5	29.2	65.9	68.9	52.1	52.2	14.8	18.0	20.9	13.5	17.1	14.4
0.22	0.28	0.28	0.36	0.38	0.26	0.25	0.10	0.15	0.18	0.16	0.20	0.17
7.10	9.56	10.22	6.09	5.63	4.63	4.66	2.77	8.29	9.82	8.91	7.61	13.62
12.7	14.7	13.2	0.2	0.0	4.7	4.7	13.1	13.8	14.8	17.1	12.0	15.0
1.58	0.57	0.54	0.07	0.16	0.37	0.34	1.58	0.80	0.62	1.03	1.40	0.71
0.95	0.08	0.16	0.01	0.02	0.07	0.08	0.78	1.06	0.50	0.71	1.59	0.60
0.23	0.51	0.18	0.02	0.03	0.04	0.04	0.11	0.17	0.06	0.17	0.19	0.19
0.68	0.15	0.00	0.64	2.70	0.29	0.22	2.50	1.91	1.25	1.45	2.18	1.28
99.6	99.8	99.8	99.8	99.9	99.7	99.6	99.8	100.4	99.5	99.6	99.3	99.7
13.35	18.10	17.60	33.60	29.30	23.50	23.60	8.21	9.66	11.10	7.65	9.89	9.20
6.66	9.41	9.61	28.56	36.37	25.98	25.97	5.68	7.26	8.58	4.95	6.06	4.22
1.44	1.20	0.87	1.34	2.16	2.20	2.30	1.71	1.87	1.77	1.49	1.79	1.50
25.7	35.2	40.8	13.1	8.9	8.7	7.2	7.9	24.3	34.8	38.2	25.0	36.1
631	852	842	1970	2390	1880	1850	473	562	710	445	482	396
7.42	10.50	7.51	43.50	33.70	22.20	107.00	96.10	130.00	221.00	152.00	591.00	321.00
95.1	122.0	115.0	248.0	233.0	181.0	183.0	64.0	83.4	94.5	76.2	75.0	86.1
92.91	35.89	34.75	153.33	71.33	280.53	419.10	124.93	168.09	195.35	127.21	205.57	164.69
1100.0	230.0	210.0	871.0	177.0	307.0	462.0	269.0	211.0	155.0	165.0	328.0	128.0
18.9	19.6	16.3	30.2	37.5	35.0	35.1	21.3	17.9	17.9	15.5	16.9	12.4
28.9	2.4	15.2	0.2	0.1	2.1	3.6	50.4	62.5	29.5	41.1	96.6	37.1
1020	211	181	15	13	636	680	1940	981	662	860	692	561
11.3	15.9	12.5	0.6	0.5	1.3	1.1	3.5	15.1	7.8	9.3	7.0	9.2
23.3	35.0	33.4	18.5	10.8	10.1	9.4	13.0	24.4	18.4	21.0	15.9	19.7
3.35	3.87	9.19	8.89	3.42	2.89	2.62	2.72	7.88	2.25	2.51	2.05	2.45
548	42	46	6	7	51	48	165	166	94	134	394	102
7.5	6.8	4.6	0.4	0.4	1.5	1.4	4.2	3.8	2.8	4.3	4.0	4.2
18.6	20.1	13.5	1.0	0.9	3.2	3.0	9.2	10.1	8.1	12.1	10.5	11.8
3.14	3.99	2.61	0.16	0.14	0.48	0.43	1.37	1.75	1.64	2.19	1.81	2.21
16.6	23.1	15.0	0.7	0.7	2.3	2.0	6.6	9.4	9.5	12.6	10.3	12.7
4.23	6.16	4.32	0.15	0.15	0.51	0.40	1.47	2.76	2.77	3.56	2.74	3.51
1.91	2.26	1.76	0.08	0.07	0.36	0.33	1.03	1.31	1.38	1.81	1.48	1.67
4.43	6.15	4.68	0.21	0.18	0.50	0.43	1.47	3.07	2.95	3.80	2.88	3.59
0.59	0.85	0.67	0.03	0.02	0.06	0.05	0.20	0.50	0.41	0.51	0.38	0.51
2.72	3.96	3.15	0.13	0.11	0.31	0.28	0.84	2.72	1.93	2.35	1.79	2.35
0.54	0.70	0.59	0.03	0.02	0.05	0.05	0.16	0.56	0.37	0.44	0.33	0.43
1.19	1.56	1.31	0.07	0.04	0.13	0.11	0.40	1.31	0.78	0.96	0.72	0.96
0.13	0.18	0.15	0.01	0.00	0.01	0.01	0.04	0.16	0.09	0.11	0.08	0.11
0.76	1.00	0.83	0.06	0.04	0.09	0.08	0.24	0.88	0.52	0.65	0.43	0.64
0.10	0.14	0.12	0.01	0.01	0.01	0.01	0.03	0.11	0.07	0.09	0.07	0.08
0.94	1.57	1.43	0.54	0.36	0.35	0.34	0.42	0.84	0.89	0.97	0.71	0.92
0.23	0.29	0.71	0.71	0.27	0.22	0.21	0.18	0.24	0.18	0.18	0.16	0.17
0.25	0.18	0.16	0.03	0.03	0.08	0.07	0.24	2.34	0.10	0.19	0.21	0.17
0.07	0.05	0.05	0.01	0.01	0.02	0.02	0.05	0.09	0.03	0.05	0.06	0.05

similar Fe^{3+}/Ti^{4+} values (0.9–1.6) and large variation in P_2O_5 (0.2–4.0 wt.%) (Fig. 7a–c, Table 2). The $Fe_2O_3(t)$ contents decrease from the base to the top in each cyclic unit consistent with decrease of the amount of Fe–Ti oxides upwards (Figs. 3, 7). The values of Fo of olivine, An of plagioclase and Mg# of clinopyroxene always decrease upwards in each cyclic unit excepting for the cyclic unit IV (Fig. 7e–f). The clinopyroxenes of the MZ rocks have low Cr and Ni concentrations (1–21 ppm and 0.4–10 ppm, respectively) relative to those of the LZ rocks.

The UZ apatite gabbro is notable by lower P_2O_5 (0.9–2.0 wt.%) and $Fe_2O_3(t)$ (4–14 wt.%) with exception for two samples and larger range of Fe^{3+}/Ti^{4+} ratios (0.4–1.6) than the MZ apatite magnetite clinopyroxenite (Fig. 7), whereas the apatite clinopyroxenite interlayer has relatively high P_2O_5 (2.4–3.3 wt.%), $Fe_2O_3(t)$ (20–28 wt.%) and Fe^{3+}/Ti^{4+} ratios (1.8).

5.4. Whole rock trace elements and Sr–Nd isotopes

As shown in primitive mantle normalized trace element diagram, similar to the LZ rocks of the Panzhihua intrusion, the Taihe LZ gabbro and olivine clinopyroxenite are characterized by positive anomalies of K, Sr and Ti, and the massive ores display positive Ti and Nb–Ta anomalies, whereas two samples have positive anomaly of Sr (Fig. 8a) (Song et al., 2013). In contrast, the MZ and UZ rocks of the Taihe intrusion show trace element compositions comparable with the UZ rocks of the Panzhihua intrusion (Fig. 8b–d) (Song et al., 2013). Most of the

Taihe MZ (apatite) magnetite clinopyroxenites show positive P, Ti and Nb–Ta anomalies and negative Sr, K, and Zr–Hf anomalies (Fig. 8b). The Taihe samples plot in the field of the Emeishan high-Ti basalts in the Sr–Nd isotope diagram with the values of $\varepsilon_{Nd\ (260\ Ma)}$ (0.3–3.6) and $(^{87}Sr/^{86}Sr)_{(260\ Ma)}$ (0.7049–0.7056) between those of the Panzhihua and Hongge intrusions (Fig. 9).

6. Discussion

Above descriptions indicate that the most impressive characters of the Taihe intrusion distinctive from the other layered intrusions in the central ELIP are: (1) the main Fe–Ti oxide ore layers comprising of thick apatite magnetite clinopyroxenites in the MZ contain as much as 5% to 12% cumulus apatite and (2) the massive Fe–Ti oxide layers occur at the top of the LZ, rather than at the base. Therefore, the key issues discussed below focus on how the massive Fe–Ti oxide formed at the top of the LZ and why the magnetite clinopyroxenite layers have so high apatite contents.

6.1. Parental magma and the formation of Lower Zone

The parental magma compositions in the Taihe intrusion are difficult to estimate because chilled margins had been damaged by intrusion of the syenite. However, the nature of the parental magma can be estimated from the composition of the cumulus minerals. The clinopyroxene is one of the important cumulus minerals throughout the Taihe intrusion. Thus trace element compositions of parental magma can be estimated by the trace element concentrations of clinopyroxene using partition coefficient of the elements between clinopyroxene and basaltic magma ($D_i^{Cpx/melt}$). The $D_i^{Cpx/melt}$ values employed in the calculation are list in Table 7 (Green et al., 2000; Hart and Dunn, 1993; Hauri et al., 1994). It is assumed that the partition coefficients are constant in the calculations, although the partition coefficients are function of compositions of the parental magma, temperature and pressure (Blundy and Wood, 2003). Fig. 10 shows the primitive mantle normalized trace elements patterns for the Taihe parental magmas comparable with those of the Emeishan high-Ti basalts, indicating a genetic linkage between them. This is agreed with the recent studies, which concluded that the layered intrusions hosting Fe–Ti oxide deposits in the ELIP are associated with evolution of the high-Ti basaltic magmas (Zhou et al., 2008).

Zhang and co-workers proposed that the layered intrusions are associated with primary picritic magma derived from partial melting of eclogite or pyroxenite in the lithospheric mantle induced by an upwelling mantle plume (Hou et al., 2011b, 2012b; Zhang et al., 2009). Study of melt inclusion in olivine phenocrysts (Fo = 88–90) of the Emeishan high-Ti picrite indicated that the primary high-Ti picritic magmas contain 6.5–19.7 wt.% MgO and ~12.2 wt.% FeO(t) (Kamenetsky et al., 2012). The FeO(t) contents of such high-Ti picritic magmas are lower than that of the typical ferropicritic magma, which contains more than 13.5 wt.% FeO(t) and 12–18 wt.% MgO (Gibson et al., 2000; Hanski and Smolkin, 1995). The Mg# of the magma in equilibrium with olivine (Fo = 71, Table 3) of the LZ olivine clinopyroxenite is ~42 according to the olivine–basaltic magma distribution coefficient $K_D = (FeO/MgO)_{olivine} / (FeO/MgO)_{liquid}$ of 0.3 (Roeder and Emslie, 1970). It is slightly lower than the Mg# of the parental magmas of the Panzhihua (47–55, Song et al., 2013), indicating that the LZ parental magmas have experienced extensive fractionation before entering the Taihe intrusion.

The trace element patterns of the LZ parental magmas in equilibrium with clinopyroxene calculated by means of $D_i^{Cpx/melt}$ values (Table 7) are flat relative to those of the MZ and UZ parental magmas (Fig. 10a), indicating more primitive parental magmas. It is consistent with the relatively high contents of Cr (65–263 ppm) and Ni (66–83 ppm) of the clinopyroxene in the LZ olivine clinopyroxenite and olivine gabbro (Table 5). Moreover, the plagioclases of the LZ rocks have An = 78–86 higher than those of the MZ (An = 51–62) (Table 4, Fig. 7). Weak negative Eu anomalies suggest that the LZ parental magma did not undergo significantly fractional crystallization of plagioclase prior to entering the Taihe intrusion (Fig. 10a). Occurrences of the olivine clinopyroxenite and gabbro in the lower part of the LZ indicate the fractional crystallization and accumulation of olivine, clinopyroxene and plagioclase after emplacement of the parental magma (Fig. 3), as a result, the residual magmas become Fe–Ti enriched. It is notable that euhedral magnetite grains may be enclosed in poikilitic clinopyroxene in the massive oxide layer (Fig. 4b), indicating early crystallization and accumulation of Fe–Ti oxides from the Fe–Ti enriched residual magma. The progressive decrease of whole rock Fe^{3+}/Ti^{4+} ratios in the massive ores suggests earlier crystallization of magnetite than ilmenite (Fig. 7c). Early crystallization of Fe–Ti oxides also resulted in Cr depletion in the residual magma and the clinopyroxene in the massive ores having Cr contents (7–22 ppm) lower than those in the beneath rocks (Cr = 65–263 ppm) (Table 5 and Fig. 7g) because the partition coefficient of Cr between magnetite and basaltic melt are as high as $D^{Cr}_{Mt/liq}$ = 50–230 (Klemme et al., 2006; Namur et al., 2010). On the other hand, the comparable An of the plagioclase (= 78–86) in the massive ores and in the olivine clinopyroxenite (An = 79–80) suggests replenishment of new Fe–Ti enriched magmas during the formation of the massive ore layer (Fig. 7e).

6.2. Fe–Ti–P enriched parental magma and the formation of the Middle Zone

6.2.1. Unusual Fe–Ti–P enriched parental magma

As described above, the MZ rocks of the Taihe intrusion are distinguished from the LZ rocks by abundance of apatite and high in P_2O_5, low in Cr and Ni and Fe^{3+}/Ti^{4+} ratios (Fig. 7). Abrupt decreases of An of the plagioclase and Ni of the clinopyroxene from the top of the LZ to the base of the MZ suggest that the MZ was formed by new pulses of more evolved magmas (Fig. 7e and h). Therefore, the parental magmas of the MZ rocks in equilibrium with the clinopyroxene are more enriched in incompatible elements than those of the LZ (e.g. light REEs, Fig. 10b–c). On the other hand, the Taihe MZ rocks have primitive mantle normalized trace element patterns evidently similar to the Upper Zone apatite gabbros of the Panzhihua intrusion, which are characterized by enrichments of P and REE and depletions of Zr and Hf (Fig. 8b–c). Song et al. (2013) recently attributed the formation of the Panzhihua Upper Zone apatite gabbros to progressive enrichment of P_2O_5 in the residual magma. However, relative to the Panzhihua Upper Zone apatite gabbros, the Taihe MZ rocks have much higher Fe_2O_3(t) contents due to accumulation of apatite together with Fe–Ti oxides (Fig. 6e). Abundant euhedral apatite grains and high percentages of Fe–Ti oxides in the MZ rocks indicate early crystallization of both apatite and Fe–Ti oxides from unusual magmas enriched in P_2O_5 as well as Fe and Ti (Fig. 4c–d).

Experimental studies have indicated that elevation of $Na_2O + K_2O + P_2O_5 + TiO_2$ in the residual magma in low pressure promotes the development of two immiscible liquids (Charlier and Grove, 2012). The more Fe-rich immiscible liquid is not only extremely enriched in Fe_2O_3, TiO_2 and P_2O_5, but also high in MgO, CaO, Zr, and REE, whereas the more silica-rich liquid has greater K_2O, Na_2O, Al_2O_3 and Rb contents (Kolker, 1982; Naslund, 1983; Philpotts, 1982; Philpotts and Doyle, 1983; Veksler et al., 2006). Reynolds (1985) and VanTongeren and Mathez (2012) argued that the nelsonite layers containing ~70% Fe–Ti-oxides and ~30% apatite in the Upper Zone of the Bushveld Complex were associated with liquid immiscible. The typical nelsonite contains one-third apatite and two-third Fe–Ti oxides (Philpotts, 1967). In contrast, the MZ apatite magnetite clinopyroxenites of the Taihe intrusion contain 10–30% Fe–Ti oxides, 5–12% apatite, and as high as 50–70% clinopyroxene and plagioclase (Figs. 3 and 4c–d). Additionally, a Fe-rich liquid would be high in density and low in viscosity, and thus would be able to percolate through silicate crystal

Table 3
Representative analyses of olivine from the Taihe intrusion.

Sample	ST11-08	ST11-09	ST11-13	ST11-15	ST11-18	ST11-25	ST11-28	ST11-42	ST11-46
Depth (m)	363	381	443	471	517	629	665	804	871
Rock	Ap Gab	Ap Mt Cpx	Ap Mt Cpx	Ap Mt Cpx	Ap Mt Cpx	Gab	Ap Mt Cpx	Ol Gab	Ol Cpx
Zone	MZ	MZ	MZ	MZ	MZ	MZ	MZ	LZ	LZ
Cyclic Unit	V	V	IV	IV	IV	II	II		
Number	4	4	4	4	4	4	4	5	4
Major elements (wt.%)									
SiO_2	38.46	40.20	39.81	39.09	40.11	39.09	38.77	39.28	39.24
TiO_2	0.09	0.16	0.06	0.06	0.08	0.04	0.06	0.06	0.06
Al_2O_3	0.02	0.01	0.01	0.02	0.01	0.01	0.01	0.01	0.01
CaO	0.05	0.04	0.05	0.06	0.06	0.06	0.05	0.04	0.05
Cr_2O_3	0.01	0.00	0.00	0.00	0.00	0.00	0.01	0.00	0.00
MgO	35.20	35.00	33.13	34.55	37.13	29.03	32.86	34.77	34.71
MnO	0.56	0.55	0.68	0.60	0.49	0.66	0.62	0.38	0.40
FeO	25.70	24.94	27.07	25.34	22.63	31.76	28.11	25.66	25.75
NiO	0.01	0.00	0.01	0.00	0.00	0.01	0.00	0.03	0.03
Total	100.09	100.89	100.81	99.73	100.52	100.67	100.50	100.24	100.25
Fo	71.15	71.64	68.77	71.05	74.70	62.19	67.78	70.92	70.81

Fo, forsterite content of olivine (atomic Mg / $(Mg + Fe^{2+}) \times 100$).

mushes (Cawthorn and Ashwal, 2009). However, such phenomenon had not been observed in the Taihe intrusion. Abundant cumulus apatites in the UZ oxide-barren gabbros (Fig. 3) suggest that the apatites were crystallized from magmas enriched in P_2O_5 and CaO. This indicates that the MZ apatite magnetite clinopyroxenites are associated with crystallization of unusual Fe–Ti–P-rich silicate

Table 4
Representative analyses of plagioclase from the Taihe intrusion.

Sample	ST11-58	ST11-56	ST11-52	ST11-08	ST11-10	ST11-11	ST11-14	ST11-18	ST11-19	ST11-20
Depth	81	113	169	363	400	415	459	517	534	558
Rock	Ap Gab	Ap Gab	Ap Gab	Ap Gab	Ap Gab	Ap Gab	Ap Mt Cpx	Ap Mt Cpx	Ap Gab	Gab
Zone	UZ	UZ	UZ	MZ	MZ	MZ	MZ	MZ	MZ	MZ
Cycle				V	IV	IV	IV	IV	III	III
Number	4	3	3	4	4	4	4	3	4	3
Major elements										
SiO_2	55.98	54.18	50.99	56.26	55.54	54.92	53.31	54.31	55.03	54.78
TiO_2	0.08	0.11	0.08	0.12	0.10	0.09	0.07	0.11	0.09	0.09
Al_2O_3	28.13	28.30	29.89	28.48	28.23	28.37	29.18	28.58	28.23	28.21
FeO	0.19	0.26	0.69	0.27	0.25	0.19	0.20	0.35	0.24	0.20
MnO	0.01	0.01	0.01	0.01	0.01	0.00	0.00	0.00	0.00	0.01
MgO	0.00	0.01	0.13	0.01	0.00	0.01	0.05	0.01	0.01	0.00
CaO	11.41	11.76	12.58	11.17	11.56	10.18	11.25	12.27	11.99	11.53
Na_2O	4.71	4.15	3.43	4.43	4.47	5.52	4.79	4.13	4.09	4.66
K_2O	0.11	0.22	1.68	0.18	0.16	0.23	0.69	0.29	0.17	0.15
Total	100.62	98.99	99.46	100.94	100.32	99.52	99.55	100.05	99.84	99.64
An	57.29	61.03	67.13	58.27	58.89	50.49	56.50	62.16	61.89	57.78

ST11-22	ST11-23	ST11-25	ST11-26	ST11-28	ST11-30	ST11-33	ST11-39	ST11-40	ST11-42	ST11-46
589	602	629	641	665	688	714	756	765	804	871
Gab	Gab	Gab	Gab	Ap Mt Cpx	Gab	Mt Cpx	Ore	Ore	Ol Gab	Ol Cpx
MZ	MZ	MZ	MZ	MZ	MZ	MZ	LZ	LZ	LZ	LZ
II	II	II	II	II	I	I				
4	3	4	3	3	3	4	4	4	2	4
53.08	56.42	55.29	55.31	56.78	54.28	53.18	46.72	50.27	50.23	50.10
0.10	0.09	0.09	0.09	0.12	0.06	0.08	0.07	0.13	0.09	0.05
29.20	27.90	28.65	28.69	27.11	28.29	29.38	31.00	32.00	32.01	31.64
0.30	0.31	0.25	0.18	0.27	0.20	0.25	0.29	0.28	0.20	0.28
0.00	0.00	0.01	0.00	0.01	0.00	0.00	0.01	0.03	0.00	0.00
0.03	0.00	0.01	0.00	0.01	0.01	0.03	0.03	0.04	0.00	0.01
12.01	11.86	12.44	12.31	10.30	11.54	11.85	18.90	15.16	15.58	15.68
4.71	4.31	4.18	4.32	5.17	4.57	4.58	1.76	2.41	2.13	2.28
0.18	0.15	0.08	0.12	0.17	0.13	0.25	0.84	0.06	0.18	0.06
99.62	101.04	100.99	101.02	99.93	99.07	99.61	99.62	100.38	100.42	100.11
58.53	60.37	62.24	61.19	52.45	58.33	58.89	85.62	77.72	80.24	79.21

An, anorthite content of plagioclase, (atomic Ca/(Ca + Na) × 100).

Table 5
Representative analyses of clinopyroxene from the Taihe intrusion.

Sample	ST11-58	ST11-56	ST11-52	ST11-51	ST11-48	ST11-02	ST11-03	ST11-05	ST11-06	ST11-08	ST11-09	ST11-10
Depth (m)	81	113	169	173	216	246	270	305	323	363	381	400
Rock	Ap Gab	Ap Gab	Ap Gab	Ap Mt Cpx	Ap Gab	Ap Mt Cpx	Ap Mt Cpx	Mt Cpx	Ap Mt Cpx	Ap Gab	Ap Mt Cpx	Ap Gab
Zone	UZ	UZ	UZ	UZ	UZ	MZ	MZ	MZ	MZ	MZ	MZ	MZ
Cyclic Unit						VI	VI	VI	VI	V	V	IV
Number	4	4	4	4	4	1	4	4	4	4	4	3
Major elements (wt.%)												
SiO_2	49.70	49.86	48.20	48.87	49.08	48.59	49.83	48.27	46.04	50.74	51.38	49.93
TiO_2	1.93	1.83	2.39	2.16	2.33	2.66	2.37	2.96	3.90	1.59	1.43	1.82
Al_2O_3	4.57	4.40	5.87	5.49	5.66	6.37	5.24	6.69	8.56	3.95	3.68	4.76
MgO	13.62	14.20	13.82	12.56	12.81	13.39	13.45	12.43	12.40	14.52	14.14	13.82
FeO	8.23	7.47	7.15	8.26	8.17	7.18	6.34	6.50	6.33	7.71	7.74	8.34
MnO	0.26	0.27	0.25	0.27	0.24	0.20	0.19	0.22	0.18	0.29	0.28	0.26
CaO	21.05	21.41	21.68	21.86	21.01	20.84	21.76	22.05	21.68	20.60	20.76	20.33
Na_2O	0.51	0.44	0.51	0.42	0.56	0.62	0.70	0.72	0.75	0.49	0.47	0.57
K_2O	0.00	0.01	0.00	0.00	0.01	0.00	0.00	0.00	0.00	0.00	0.00	0.02
Total	99.88	99.88	99.87	99.87	99.87	99.87	99.88	99.84	99.84	99.89	99.89	99.86
Mg#	74.86	77.38	77.67	73.25	73.83	77.06	79.25	77.48	77.90	77.21	76.68	74.89
Trace elements (ppm)												
Sc	64.03	60.28	52.06	54.05	53.30	47.85	62.52	49.44	43.53	64.53	65.29	63.06
V	241.16	225.42	221.84	216.42	241.65	231.49	209.35	284.80	220.67	202.77	191.09	243.30
Cr	1.61	1.38	4.05	16.65	0.63	2.31	2.74	14.37	3.89	5.69	2.02	20.03
Co	25.46	24.76	21.85	23.06	23.74	21.32	18.46	21.12	15.66	22.04	24.93	29.57
Ni	7.56	0.86	1.38	1.58	1.56	0.65	0.15	45.89	0.36	0.48	0.47	0.64
Cu	0.21	0.42	0.39	0.27	0.31	0.12	0.38	0.65	0.53	0.41	0.37	5.08
Ga	8.29	8.12	9.10	8.95	8.94	8.62	7.26	9.91	9.93	7.56	7.07	8.56
Rb	0.03	0.11	0.03	0.11	0.17	0.06	0.03	0.30	0.20	0.16	0.01	0.46
Sr	150.08	148.43	197.20	211.26	202.42	243.15	234.73	275.97	421.35	146.55	141.53	162.58
Y	28.62	25.92	29.80	27.99	27.05	29.36	33.20	32.46	37.30	25.65	26.10	26.60
Zr	35.62	32.64	45.64	42.31	42.18	45.10	37.63	63.21	60.58	23.01	24.83	30.17
Nb	0.28	0.15	0.35	0.35	0.30	0.46	0.32	0.69	0.93	0.10	0.08	0.70
Ba	0.63	3.50	1.49	2.05	3.28	0.43	1.14	1.99	6.11	1.92	1.18	17.11
La	4.95	4.94	6.67	6.76	5.59	7.65	7.81	9.32	10.93	4.49	4.33	5.32
Ce	21.74	20.89	28.13	27.56	24.33	29.49	32.57	35.61	42.95	19.71	19.11	22.81
Pr	4.63	4.62	5.91	5.63	5.25	5.95	6.93	6.99	8.33	4.56	4.51	4.82
Nd	29.20	29.64	38.06	34.82	32.96	38.84	47.76	46.78	53.11	29.45	29.63	31.04
Sm	9.14	8.70	10.22	9.78	9.52	10.09	12.72	10.70	12.98	9.35	9.61	10.35
Eu	3.39	3.25	3.94	3.54	3.80	4.86	6.09	4.25	5.11	3.45	3.31	3.26
Gd	8.92	8.98	10.98	10.08	10.09	11.58	14.31	12.60	14.71	10.13	10.29	9.62
Tb	1.37	1.25	1.44	1.27	1.30	1.34	1.73	1.59	1.76	1.34	1.33	1.27
Dy	7.25	6.56	7.99	7.00	7.09	8.33	9.61	9.21	10.45	7.03	7.28	7.33
Ho	1.21	1.10	1.28	1.25	1.26	1.38	1.67	1.57	1.84	1.12	1.10	1.17
Er	2.58	2.94	3.26	2.82	2.78	2.65	3.07	3.61	4.05	2.61	2.75	2.87
Tm	0.34	0.29	0.32	0.34	0.30	0.34	0.36	0.35	0.41	0.26	0.29	0.29
Yb	1.65	1.77	1.78	1.71	1.57	1.77	1.94	2.02	2.24	1.57	1.76	1.77
Lu	0.22	0.23	0.25	0.25	0.24	0.23	0.25	0.28	0.29	0.20	0.22	0.22
Hf	1.36	1.37	1.94	1.69	1.68	1.80	1.80	2.34	2.06	1.19	1.16	1.32
Ta	0.04	0.04	0.08	0.07	0.07	0.11	0.07	0.15	0.24	0.03	0.03	0.07
Th	0.06	0.03	0.05	0.07	0.04	0.07	0.04	0.12	0.11	0.02	0.02	0.07
U	0.02	0.04	0.01	0.04	0.05	0.01	0.02	0.06	0.04	0.13	0.02	0.07

Mg#, atomic Mg / $(Mg + Fe^{2+} + Fe^{3+}) \times 100$.

magmas, rather than with nelsonitic magma. Similarly, the formation of the MCU I (megacyclic units I) apatite-bearing ferrogabbros of the Sept Iles intrusion, Canada, was attributed to fractional crystallization of a homogeneous magma (Namur et al., 2012).

6.2.2. Origin of the Fe–Ti–P enriched parental magma

Experiments have indicated that phosphate saturation in natural basaltic magma should occur in very late stage of fractionation when the residual liquid contains more than 1.3 wt.% P_2O_5, and the liquidus temperature of apatite is commonly lower than that of magnetite and ilmenite (Tollari et al., 2006). The study of the melt inclusions in the olivine phenocrysts of the Emeishan high-Ti picrites indicated that the primary picritic magmas contain P_2O_5 as low as 0.33 wt.% (Kamenetsky et al., 2012). Thus, ~75% of fractional crystallization of silicates and Fe–Ti oxides is needed for the P_2O_5 contents to reach phosphate saturation in the residual magma of the Panzhihua intrusion (Song et al., 2013). Such highly differentiated residual magma is characterized by enrichment of P, Si and Al and moderate depletion of Mg, Fe and Ti and associated with the formation of the Upper Zone apatite gabbros of the Panzhihua intrusion, which have low contents of Fe–Ti oxides. Therefore, the unusual Fe–Ti–P-rich mafic magma for the Taihe MZ apatite magnetite clinopyroxenes cannot be created by means of extensive fractionation of picritic magma.

Recent studies have indicated that the Fe–Ti enriched magma genetically associated with the Fe–Ti oxide layers in the Panzhihua and Baima intrusions were produced by extensive fractional crystallization of olivine, clinopyroxene and plagioclase of picritic magma at depths

ST11-11	ST11-13	ST11-14	ST11-15	ST11-17	ST11-18	ST11-19	ST11-20	ST11-21	ST11-22	ST11-23	ST11-25
415	443	459	471	506	517	534	558	575	589	602	629
Ap Gab	Ap Mt Cpx	Ap Mt Cpx	Ap Mt Cpx	Ap Mt Cpx	Ap Mt Cpx	Ap Gab	Gab	Ap Mt Cpx	Gab	Gab	Gab
MZ	MZ	MZ	MZ	MZ	MZ	MZ	MZ	MZ	MZ	MZ	MZ
IV	IV	IV	IV	IV	IV	III	III	III	II	II	II
4	4	4	4	3	4	4	4	4	4	4	3
50.37	50.93	50.39	50.33	50.42	50.68	49.74	50.68	50.20	49.99	50.97	50.69
1.68	1.57	1.56	1.70	1.61	1.41	1.56	1.35	1.92	2.03	1.69	1.78
4.14	3.83	4.02	4.10	4.13	3.53	4.26	3.68	4.55	4.91	4.18	4.36
13.46	14.11	14.64	13.97	14.48	15.03	14.46	13.91	12.95	12.65	13.82	14.14
9.14	8.04	7.69	7.96	7.59	7.77	8.05	8.16	7.85	7.87	8.09	7.79
0.28	0.30	0.28	0.29	0.29	0.33	0.27	0.29	0.23	0.22	0.25	0.25
20.19	20.52	20.83	21.02	20.84	20.65	21.02	21.27	21.67	21.71	20.39	20.36
0.61	0.58	0.48	0.51	0.53	0.50	0.48	0.48	0.51	0.50	0.47	0.49
0.01	0.00	0.00	0.00	0.00	0.00	0.01	0.04	0.00	0.00	0.00	0.00
99.89	99.89	99.89	99.88	99.88	99.89	99.84	99.87	99.88	99.87	99.87	99.87
72.60	75.95	77.42	75.96	77.45	77.73	76.37	75.41	74.81	74.32	75.45	76.56
65.44	68.04	66.52	67.09	64.83	68.11	65.48	66.60	67.67	70.33	66.23	66.28
196.15	192.77	201.57	212.94	219.13	168.48	229.07	235.92	276.02	296.33	257.10	261.86
7.77	10.47	1.70	2.77	11.28	1.27	10.15	81.09	7.30	0.93	5.14	4.65
23.86	22.25	24.14	24.96	25.93	24.34	29.37	29.21	29.81	31.34	30.15	29.99
1.77	0.61	0.66	0.46	0.71	0.55	1.69	9.03	9.57	10.55	11.04	10.23
0.46	0.38	0.54	0.28	0.56	0.45	0.89	0.66	0.64	0.36	0.34	0.32
8.06	7.47	7.32	7.32	7.26	7.19	8.31	7.41	8.26	8.93	7.96	7.82
0.53	0.13	0.11	0.04	0.04	0.03	0.38	0.46	0.10	0.06	0.03	0.09
137.89	133.84	136.44	139.04	135.58	141.13	126.83	105.56	127.76	128.75	125.79	127.01
27.71	26.65	26.40	28.93	28.52	31.14	26.76	26.63	19.93	19.80	23.21	22.49
23.78	25.12	26.13	26.46	26.51	33.67	33.72	38.28	26.32	32.89	30.90	30.72
0.14	0.09	0.13	0.10	0.11	0.13	0.19	0.21	0.11	0.14	0.15	0.15
2.03	1.88	0.95	0.91	0.50	0.62	3.12	6.22	1.06	0.57	0.83	0.95
4.33	4.93	4.27	4.85	4.91	4.85	4.77	6.28	3.35	3.42	4.86	5.31
20.94	21.53	19.24	21.55	21.11	21.46	20.82	23.22	14.87	14.75	18.62	20.24
4.72	4.55	4.31	4.75	4.66	4.77	4.43	4.47	3.17	3.18	3.82	4.04
30.51	30.99	29.93	32.70	30.48	31.93	29.12	29.00	22.63	22.95	22.86	23.54
10.79	9.28	9.07	9.77	9.28	9.97	9.20	9.16	7.91	7.48	7.85	7.97
3.22	3.34	2.96	3.16	3.27	3.46	3.21	2.71	2.30	2.41	2.61	2.52
9.52	9.32	10.04	10.66	10.70	11.64	9.38	8.98	7.08	7.03	8.78	8.75
1.29	1.26	1.30	1.37	1.27	1.44	1.39	1.37	0.99	1.10	1.08	1.13
7.69	7.13	6.88	7.48	7.22	7.46	6.69	6.61	5.10	5.40	5.52	5.48
1.23	1.21	1.17	1.22	1.20	1.30	1.10	1.05	0.85	0.86	1.04	1.04
2.93	2.87	2.87	3.10	2.66	3.08	2.78	2.58	2.11	2.26	2.16	2.27
0.30	0.34	0.29	0.32	0.32	0.37	0.33	0.31	0.23	0.26	0.24	0.23
1.82	1.63	1.85	1.88	1.86	2.12	1.89	1.80	1.29	1.46	1.68	1.61
0.22	0.21	0.20	0.20	0.27	0.32	0.28	0.31	0.16	0.15	0.19	0.19
1.07	1.21	1.23	1.17	1.26	1.66	1.48	1.62	1.21	1.59	1.29	1.40
0.03	0.02	0.03	0.03	0.04	0.04	0.06	0.04	0.03	0.03	0.04	0.05
0.04	0.03	0.04	0.04	0.06	0.04	0.06	0.23	0.04	0.05	0.15	0.11
0.03	0.01	0.04	0.03	0.03	0.09	0.09	0.09	0.02	0.01	0.03	0.04

(*continued on next page*)

(Pang et al., 2008; Song et al., 2013; Zhang et al., 2012). Thus, a possible process to form the Fe–Ti–P-rich mafic magma is input of phosphorous via crustal contamination during ascending of a Fe–Ti enriched magma. However, Sr–Nd isotopic values of the Taihe intrusive rocks shown in Table 6 display a weak crustal contamination (Fig. 9). Alternatively, the similar trace element compositions between the Taihe MZ rocks and the Panzhihua Upper Zone apatite gabbros permit us to speculate the existence of a magma chamber in the middle level between the deep-seated magma chamber and the Taihe intrusion.

It is reasonable to assume that the magma that remains in the upper part of the middle level magma chamber is enriched in P, Si, Al and incompatible elements and moderately depleted in Mg, Fe and Ti after extensive fractional crystallization of silicates and Fe–Ti oxides, like the residual magma forming the Upper Zone apatite gabbros of the Panzhihua intrusion. If the magma conduit between the deep-seated magma chamber and the Taihe intrusion was closely adjacent to the middle level magma chamber, the wall rocks of the middle level magma chamber may be progressively eroded by the hot Fe–Ti enriched magma derived from the deep-seated chamber. Thus, the hot Fe–Ti enriched magma may mix with the highly evolved P-enriched residual magma that remained in the upper part of the middle level chamber. In addition, the hot magma from deep level may melt some of fusible minerals, such as magnetite and ilmenite and apatite, in the middle level chamber, because these oxides and apatite have relatively low liquidus temperature (Tollari et al., 2006; Toplis and Carroll, 1995). This process can produce the Fe–Ti–P enriched magmas as shown in Fig. 12. We speculate that when the Fe–Ti–P enriched magmas from the middle level magma chamber intrude into the Taihe intrusion,

Table 5 (*continued*)

Sample	ST11-26	ST11-27	ST11-28	ST11-29	ST11-30	ST11-32	ST11-33	ST11-39	ST11-40	ST11-42	ST11-44	ST11-46
Depth (m)	641	653	665	677	688	698	714	756	765	804	839	871
Rock	Gab	Ap Mt Cpx	Ap Mt Cpx	Ap Mt Cpx	Gab	Mt Cpx	Mt Cpx	Ore	Ore	Ol Gab	Gab	Ol Cpx
Zone	MZ	MZ	MZ	MZ	MZ	MZ	MZ	LZ	LZ	LZ	LZ	LZ
Cyclic Unit	II	II	II	II	I	I	I					
Number	4	4	4	4	4	4	4	4	4	4	4	5
Major elements (wt.%)												
SiO_2	48.46	49.29	50.86	48.99	49.47	47.43	50.78	47.38	48.46	47.92	49.65	48.59
TiO_2	1.83	2.05	1.51	2.18	1.77	2.84	2.01	2.41	2.21	2.21	1.83	2.18
Al_2O_3	4.67	4.90	3.57	5.23	4.53	6.52	5.12	5.96	6.21	5.97	4.86	5.85
MgO	13.75	13.26	14.64	13.69	13.83	12.41	13.06	14.07	13.49	13.45	13.99	13.98
FeO	9.52	8.70	7.45	7.89	8.37	7.97	7.78	7.51	7.03	7.56	7.26	6.53
MnO	0.23	0.19	0.30	0.19	0.24	0.18	0.20	0.15	0.13	0.15	0.18	0.16
CaO	20.91	20.98	21.01	21.17	21.14	21.95	20.37	21.81	21.78	22.02	21.66	22.10
Na_2O	0.49	0.50	0.54	0.52	0.53	0.56	0.55	0.57	0.54	0.58	0.43	0.43
K_2O	0.00	0.00	0.00	0.00	0.00	0.00	0.00	0.00	0.00	0.00	0.00	0.01
Total	99.87	99.87	99.88	99.86	99.87	99.86	99.87	99.85	99.86	99.85	99.86	99.83
Mg#	72.22	73.29	77.96	75.74	74.84	73.70	75.14	77.15	77.55	76.22	77.63	79.41
Trace elements (ppm)												
Sc	68.27	67.23	60.59	69.20	69.95	64.77	69.61	82.73	74.05	78.41	72.80	73.01
V	281.33	286.42	195.38	305.81	271.52	326.21	290.69	356.63	338.87	339.02	287.27	309.17
Cr	10.03	2.74	3.61	15.04	2.51	2.47	9.39	7.28	21.76	76.44	65.04	263.26
Co	31.77	30.82	18.25	30.83	30.95	30.29	30.42	34.19	33.36	32.45	31.93	30.12
Ni	8.98	1.56	0.68	2.48	9.61	5.90	7.29	57.44	72.75	83.13	70.42	65.64
Cu	0.57	0.59	0.63	0.42	0.63	0.31	0.26	0.32	0.46	0.52	0.50	0.62
Ga	8.47	8.76	7.17	8.92	8.26	10.79	8.70	10.95	10.18	9.29	8.40	8.92
Rb	0.19	0.09	0.07	0.08	0.30	0.05	0.10	0.15	0.06	0.06	0.20	0.17
Sr	125.37	135.04	179.05	133.38	126.65	147.69	142.69	144.17	144.46	129.06	118.47	128.49
Y	23.00	21.00	25.78	20.58	21.88	20.25	18.08	16.98	13.60	14.10	15.73	14.73
Zr	33.31	29.30	23.23	36.99	34.07	42.74	26.58	29.80	26.26	27.97	36.30	29.25
Nb	0.17	0.14	0.17	0.17	0.25	0.35	0.16	0.13	0.23	0.16	0.20	0.24
Ba	0.29	3.03	1.31	2.23	1.12	0.90	0.44	1.14	0.75	0.82	1.12	2.19
La	6.59	3.80	4.89	4.07	5.22	4.84	3.22	3.43	2.75	2.71	4.22	3.49
Ce	23.17	16.65	22.10	17.61	19.47	18.94	13.28	14.27	11.42	11.78	15.14	12.92
Pr	4.46	3.61	4.66	3.77	4.26	4.31	2.93	2.91	2.45	2.56	3.00	2.65
Nd	26.76	24.49	32.30	25.08	25.26	25.40	18.31	18.99	16.00	16.15	18.01	16.61
Sm	7.51	7.63	9.47	7.86	7.52	7.38	6.15	6.46	5.39	5.99	5.75	5.56
Eu	2.72	2.66	3.87	2.79	2.89	2.87	2.30	2.38	2.10	2.18	2.15	2.08
Gd	8.08	7.95	10.51	8.42	7.63	7.30	6.11	6.38	5.48	6.07	6.59	6.42
Tb	1.08	1.03	1.28	1.10	1.08	1.04	0.82	0.82	0.76	0.76	0.75	0.69
Dy	5.98	5.64	7.65	6.08	5.91	5.41	4.84	4.50	3.61	3.72	3.85	3.93
Ho	0.93	0.89	1.18	0.96	0.98	0.88	0.74	0.70	0.66	0.67	0.69	0.63
Er	2.43	2.22	2.68	2.19	2.33	2.12	1.96	1.74	1.42	1.55	1.50	1.41
Tm	0.26	0.22	0.32	0.25	0.23	0.21	0.20	0.20	0.15	0.17	0.18	0.17
Yb	1.51	1.22	1.83	1.61	1.68	1.34	1.15	1.04	0.99	1.07	1.11	1.04
Lu	0.20	0.15	0.22	0.18	0.19	0.16	0.14	0.15	0.14	0.12	0.14	0.14
Hf	1.40	1.40	0.98	1.72	1.56	2.14	1.25	1.41	1.32	1.36	1.60	1.32
Ta	0.04	0.03	0.03	0.05	0.05	0.07	0.03	0.04	0.03	0.04	0.04	0.04
Th	0.24	0.03	0.03	0.06	0.14	0.10	0.05	0.10	0.09	0.05	0.11	0.09
U	0.05	0.04	0.03	0.01	0.08	0.04	0.03	0.03	0.03	0.04	0.04	0.03

magnetite, ilmenite and apatite can crystallize early together with clinopyroxene to form the apatite magnetite clinopyroxenite at the bases of each cyclic unit (Fig. 3). The Upper Zone apatite gabbros of the Panzhihua intrusion not only are high in P_2O_5, but also low in Fe^{3+}/Ti^{4+} ratios relative to the Lower and Middle Zones, indicating they have lower ratios between magnetite and ilmenite (Song et al., 2013). Thus, the MZ rocks of the Taihe intrusion crystallized from the Fe–Ti–P enriched magma plot on the same trend as the Upper Zone apatite gabbros of the Panzhihua intrusion in the diagrams of Fe_2O_3(t) versus P_2O_5 and TiO_2 (Fig. 6a and e). This model can explain why the Taihe MZ rocks have primitive mantle normalized trace elements patterns similar to the Upper Zone gabbro of the Panzhihua intrusion (Fig. 8b–c). Furthermore, the clinopyroxenes of some apatite magnetite clinopyroxenites in the Cycle VI of MZ show higher Zr, Ti and Ce concentrations than clinopyroxenes of the UZ samples, strongly suggesting a replenishment of magma enriched Fe, Ti and P, as well as incompatible elements (Figs. 10b, 11a–b).

6.2.3. Magma replenishment and the formation of the MZ

In the MZ of the Taihe intrusion, the periodically compositional reversals in Fo of olivine, An of plagioclase and Mg# in clinopyroxene (Fig. 7d–f) clearly demonstrate the multiple magma replenishment. The occurrence of the apatite magnetite clinopyroxenite at the bases of the cyclic units in the MZ can be attributed to the replenishment of Fe–Ti–P-rich magma. Moreover, the MZ rocks have lower Fe^{3+}/Ti^{4+} ratios than massive ores of the LZ (Fig. 7c), indicating that the apatite magnetite clinopyroxenites have relatively higher ilmenite/magnetite ratios. This feature may have resulted from the resorption of ilmenite by the hot hybrid magma from the middle level chamber, because

Table 6
Rb–Sr and Sm–Nd isotopic compositions in whole rock from the Taihe intrusion.

Sample	Rock	Zone	Cycle	Rb (ppm)	Sr (ppm)	$^{87}Sr/^{86}Sr$	2σ	$(^{87}Sr/^{86}Sr)_i$	Sm (ppm)	Nd (ppm)	$^{143}Nd/^{144}Nd$	2σ	$(^{143}Nd/^{144}Nd)_i$	$\varepsilon_{Nd}(t)$
ST11-56	Ap Gab	UZ		40.40	1720	0.705328	0.000011	0.705077	8.99	41.90	0.512656	0.000010	0.512435	2.58
ST11-51	Ap Mt Cpx	UZ		1.91	743	0.704941	0.000013	0.704914	17.80	79.30	0.512661	0.000009	0.512430	2.48
ST11-48	Ap Gab	UZ		52.10	2000	0.705281	0.000018	0.705002	9.61	41.90	0.512659	0.000009	0.512423	2.34
ST11-03	Ap Mt Cpx	MZ	V	0.66	476	0.705544	0.000008	0.705529	15.60	69.30	0.512647	0.000008	0.512416	2.19
ST11-06	Ap Mt Cpx	MZ	V	7.68	904	0.705301	0.000013	0.705210	17.80	81.60	0.512635	0.000008	0.512411	2.10
ST11-09	Ap Mt Cpx	MZ	IV	0.54	244	0.705108	0.000013	0.705084	15.30	67.10	0.512630	0.000008	0.512396	1.80
ST11-10	Gab	MZ	III	10.30	1230	0.705165	0.000011	0.705075	11.70	52.80	0.512672	0.000010	0.512444	2.75
ST11-13	Ap Mt Cpx	MZ	III	9.17	419	0.705214	0.000013	0.704980	17.60	75.80	0.512655	0.000009	0.512416	2.21
ST11-14	Ap Mt Cpx	MZ	III	1.18	316	0.705188	0.000011	0.705148	14.00	58.20	0.512683	0.000011	0.512436	2.58
ST11-16	Ap Mt Cpx	MZ	III	0.83	275	0.705222	0.000013	0.705190	13.60	58.40	0.512664	0.000011	0.512425	2.37
ST11-17	Ap Mt Cpx	MZ	III	3.18	286	0.705110	0.000017	0.704991	12.20	50.30	0.512648	0.000010	0.512399	1.86
ST11-21	Ap Mt Cpx	MZ	II	3.79	333	0.705356	0.000014	0.705234	9.74	38.50	0.512652	0.000010	0.512392	1.73
ST11-22	Gab	MZ	II	12.60	627	0.705198	0.000013	0.704983	4.53	18.00	0.512690	0.000010	0.512431	2.50
ST11-25	Gab	MZ	II	13.00	789	0.705110	0.000010	0.704934	4.13	15.50	0.512701	0.000009	0.512427	2.42
ST11-27	Ap Mt Cpx	MZ	II	0.52	200	0.705143	0.000010	0.705115	10.20	43.20	0.512676	0.000010	0.512433	2.54
ST11-29	Ap Mt Cpx	MZ	II	0.59	201	0.704995	0.000017	0.704964	10.20	45.50	0.512662	0.000010	0.512432	2.50
ST11-30	Gab	MZ	I	28.90	1020	0.705665	0.000018	0.705362	4.23	16.60	0.512678	0.000009	0.512416	2.20
ST11-33	Mt Cpx	MZ	I	15.20	181	0.706043	0.000011	0.705145	4.32	15.00	0.512701	0.000009	0.512405	1.98
ST11-42	Ol Gab	LZ		62.50	981	0.705724	0.000014	0.705042	2.76	9.41	0.512682	0.000011	0.512380	1.51
ST11-44	Gab	LZ		41.10	860	0.705689	0.000013	0.705178	3.56	12.60	0.512668	0.000008	0.512377	1.45
ST11-46	Ol Cpx	LZ		37.10	561	0.705702	0.000014	0.704995	3.51	12.70	0.512705	0.000010	0.512421	2.30

ilmenite has relatively low crystallizing temperature (Toplis and Carroll, 1995).

For the MZ rocks containing P_2O_5 more than 1.0 wt.%, P_2O_5 is positively correlated with $Fe_2O_3(t)$ (Fig. 6e). Recent experimental results of Tollari et al. (2006) indicated that crystallization of apatite dominantly depends on enrichment of P_2O_5 and CaO in magma, whereas crystallization of Fe–Ti oxides strongly depends on FeO, Fe_2O_3, and TiO_2 contents in the magma, although oxygen fugacity also play an important role. On the other hand, experiment of Toplis et al. (1994) indicated that occurrence of Fe^{3+}–P complexes in magmas could obstruct early crystallization of magnetite and promote enrichment of Fe in magma. This means that the early crystallization of apatite and Fe–Ti oxides in the Taihe MZ needs the magma to be unusually enriched not only in P_2O_5 and CaO but also in FeO, Fe_2O_3, and TiO_2. Relatively early crystallization of apatite from such Fe–Ti–P enriched magma would trigger saturation of magnetite and results in accumulation of them almost simultaneously (Tollari et al., 2008). Thus, the formation of the apatite magnetite clinopyroxenites at the bases of each cyclic unit of the MZ can be interpreted by early crystallization and accumulation of abundant apatite and Fe–Ti oxides together with clinopyroxene from the Fe–Ti–P-rich replenished magma in the Taihe magma chamber. The plagioclase crystallizes late from the residual magma relatively depleted in Fe and Ti and therefore apatite gabbros occur in the upper part of each cyclic unit. Moreover, the plagioclase has lower density ($\rho = 2.6$) than the Fe–Ti oxides ($\rho_{Mt} = 5.2$ and $\rho_{Ilm} = 4.7$) and clinopyroxene ($\rho = 3.3$–3.5) and apatite ($\rho = 3.1$–3.3) resulting in its remaining stagnant in the magma during the mafic minerals and apatite settling by gravity.

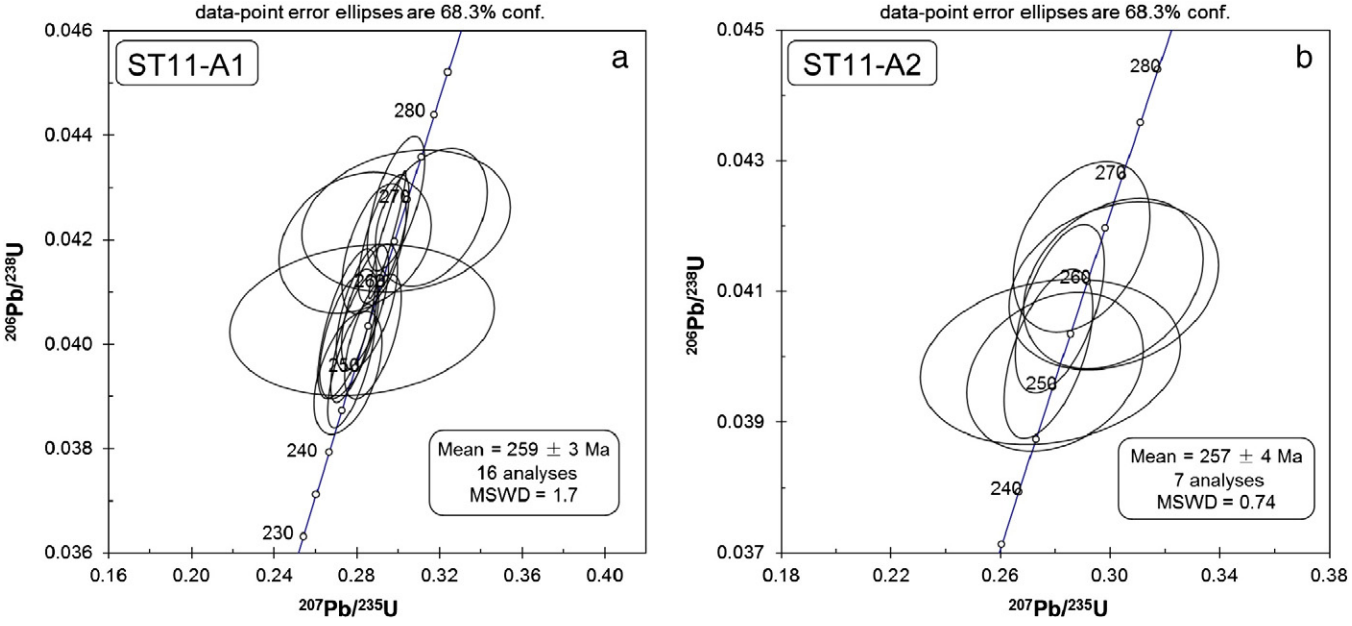

Fig. 5. Concordia diagrams of SHRIMP zircon U–Pb analyses of the zircon separate from the Taihe intrusion (ST11-A1 and ST11-A2).

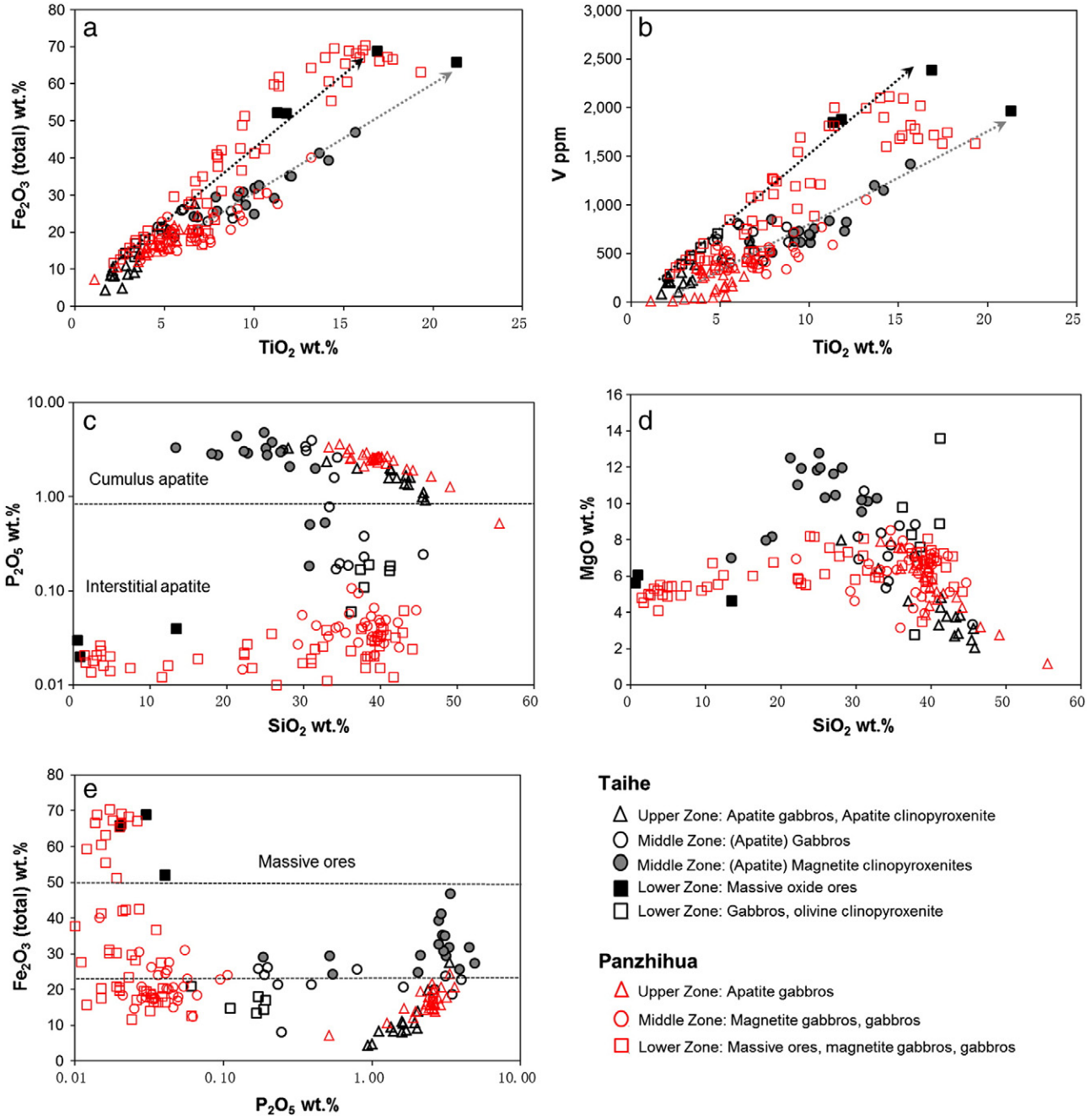

Fig. 6. (a and b) Binary plots of TiO_2 of whole rock vs Fe_2O_3(t) and V of whole rock, respectively; (c and d) binary plots of SiO_2 of whole rock vs P_2O_5 and MgO of whole rock, respectively; (e) binary plots of P_2O_5 of whole rock vs Fe_2O_3(t) of whole rock.
The data of the Panzhihua intrusion is after Song et al. (2013).

6.3. The formation of the Upper Zone

The UZ of the Taihe intrusion is distinguished from the MZ by higher proportion of plagioclase (Fig. 3) and lower Fe_2O_3(t) and P_2O_5 contents (Fig. 7a–b), comparable with the Upper Zone apatite gabbros of the Panzhihua intrusion (Figs. 6, 8d) (Song et al., 2013). The UZ apatite gabbros have relatively low Fe_2O_3(t) and TiO_2 contents, and high SiO_2 and Al_2O_3 content of whole rock indicating that the parental magma has experienced extensive fractionation of Fe–Ti oxides (Table 2). Therefore, it can be concluded that the apatite gabbros of the UZ resulted from crystallization of derivative liquids due to the fractionation of mafic silicates and Fe–Ti oxides after the formation of the MZ, although the appearance of the thin apatite clinopyroxenite interlayer suggest a weak magma replenishment. Such highly differentiated magmas are relatively enriched in SiO_2 and Al_2O_3, and depleted in TiO_2, Fe_2O_3 and MgO.

7. Conclusions

The Taihe intrusion was formed at 259 ± 3 Ma, together with the other layered intrusions in the central ELIP due to the mantle plume activity. The massive Fe–Ti oxide layer at the top of the Lower Zone of the intrusion was formed by early crystallization and accumulation of Fe–Ti

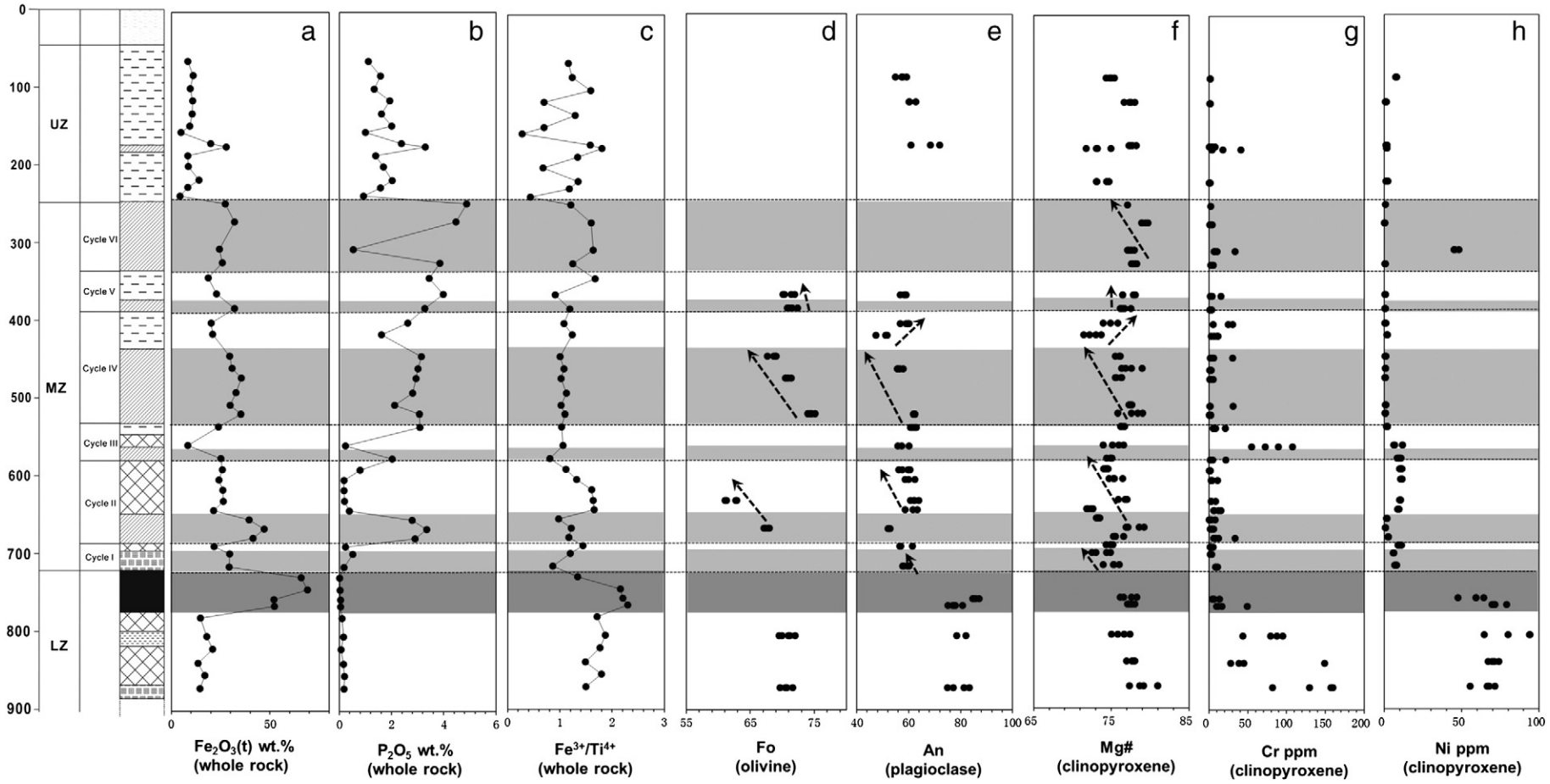

Fig. 7. Chemostratigraphic columns of whole rock major oxides, ratios of Fe^{3+}/Ti^{4+}, and Fo of olivine, An of plagioclase and Mg# as well as Cr and Ni contents in clinopyroxene of the Taihe intrusion.

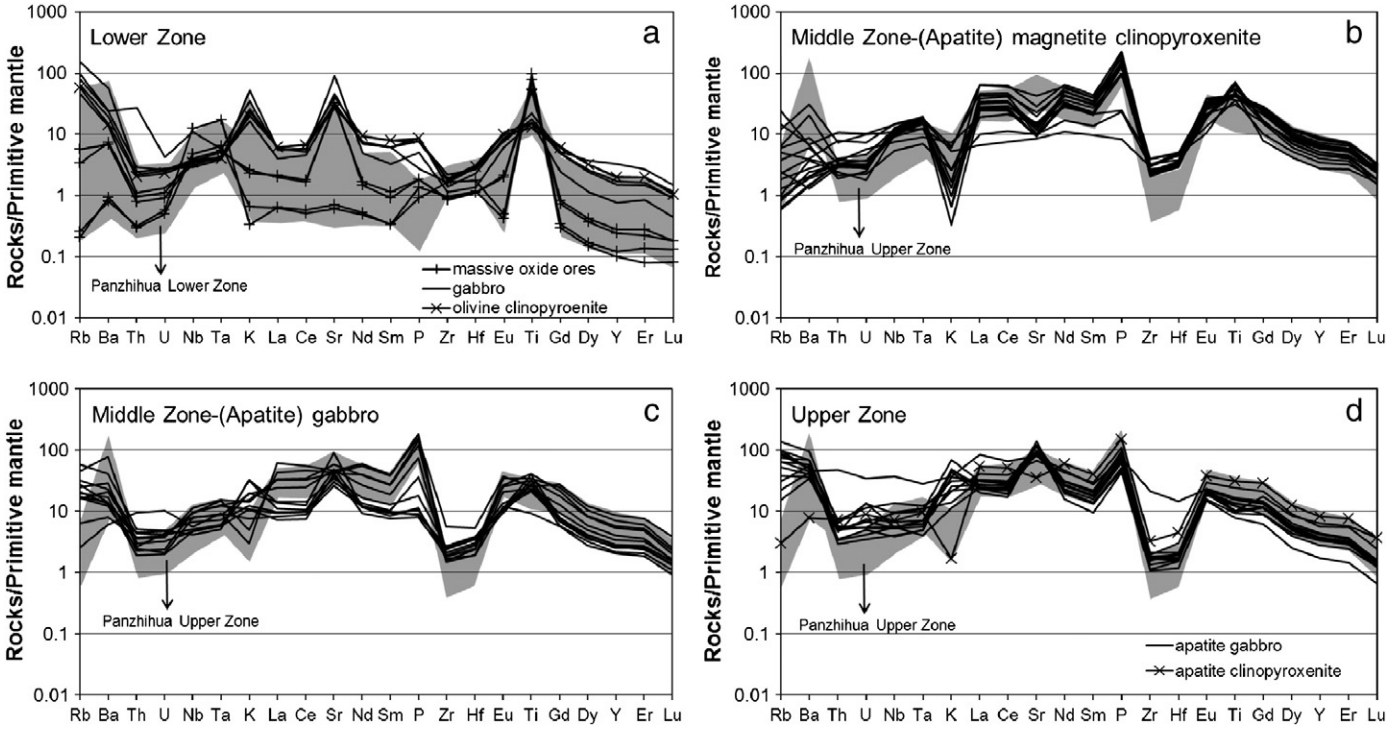

Fig. 8. Primitive mantle normalized trace element patterns of the Taihe rocks.
Normalization values are from Sun and McDonough (1989). Shaded regions indicate the different rocks of the Panzhihua intrusion after Song et al. (2013).

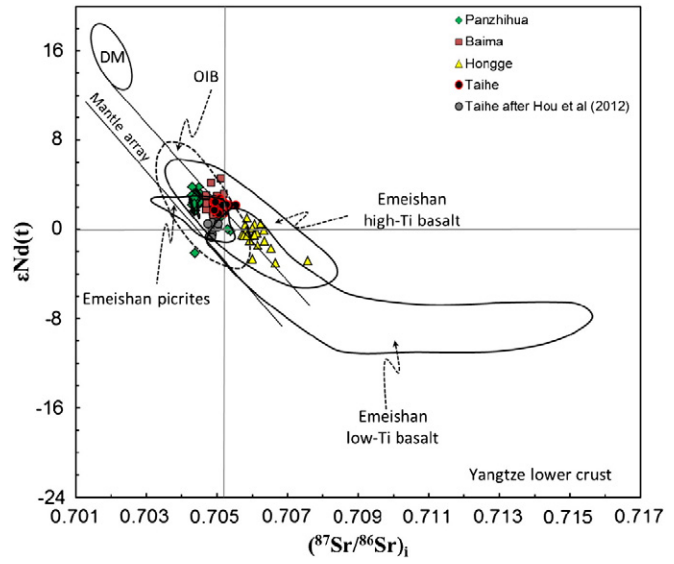

Fig. 9. Plot of initial $\varepsilon_{Nd}(t)$ versus $(^{87}Sr/^{86}Sr)_i$ (t = 260 Ma) for the Taihe intrusive rocks. Different fields denote Sr–Nd isotopic compositions of volcanic rocks in the Emeishan large igneous province after Chung and Jahn (1995), Zhang et al. (2006), Xu et al. (2001), Xiao et al. (2004), Zhou et al. (2006), Wang et al. (2007), Song et al. (2008) and Qi and Zhou (2008). The Sr–Nd isotopic data of ore-bearing intrusions are from Pang et al. (2010), Song et al. (2013), Zhang et al. (unpublished data), Luan et al. (2013–this issue) and Hou et al. (2012a).

oxides from the residual magma after fractionation of clinopyroxene and plagioclase. The Middle Zone of the intrusion was formed by crystallization of unusual Fe–Ti–P enriched magmas, which, in turn, were produced by mixing of Fe–Ti enriched magmas from a deep-seated magma chamber with highly evolved P-rich magmas in a middle level magma chamber. Early crystallization and accumulation of magnetite, ilmenite and apatite from the Fe–Ti–P enriched magmas resulted in the formation of the apatite magnetite clinopyroxenites at the bases of the cyclic units. The Upper Zone apatite gabbro is the result of the crystallization of the derivative magma after the formation of the Middle Zone.

Acknowledgments

This study was funded by the National Basic Research Program of China (2012CB416804) and research grants from State Key Laboratory of Ore Deposit Geochemistry (SKLOG-ZY125-06) and NSFC research grants (40730420) to Xie-Yan Song. We thank Zhou Guo-Fu and Liu Shi-Rong for the microprobe analysis. We acknowledge Li Liang for the LA-ICP-MS analysis. Ms. Hu Jing and Huang Yan are thanked for their efforts in trace element analysis.

Table 7
Clinopyroxene-melt partition coefficients of selected trace elements.

	Th	Nb	La	Ce	Sr	Nd	Sm	Zr	Eu	Ti	Y	Er	Lu
$D_i^{Cpx/melt}$	0.014	0.0081	0.0515	0.108	0.157	0.277	0.462	0.043	0.458	0.451	0.467	0.66	0.623
Ref.	(2)	(2)	(2)	(2)	(2)	(2)	(2)	(3)	(2)	(2)	(1)	(2)	(2)

References: (1) Hart and Dunn (1993), (2) Hauri et al. (1994) and (3) Green et al. (2000).

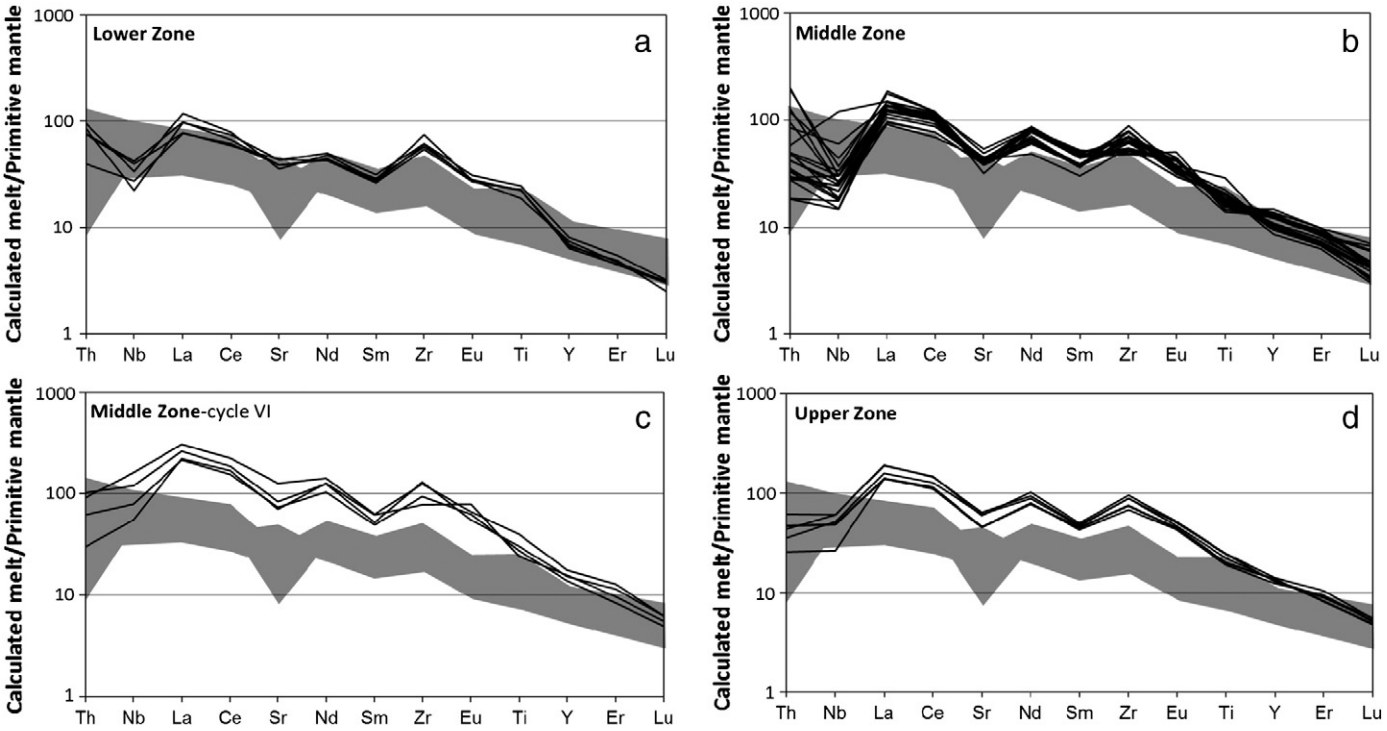

Fig. 10. Primitive mantle normalized trace elements patterns of the melts in equilibrium with clinopyroxene of the Taihe intrusive rocks. Partition coefficient values are from Hart and Dunn (1993), Hauri et al. (1994) and Green et al. (2000). Shaded regions indicate Emeishan high-Ti basalts after Xu et al. (2001), Xiao et al. (2004) and Song et al. (2008). The values of primitive mantle are from Sun and McDonough (1989).

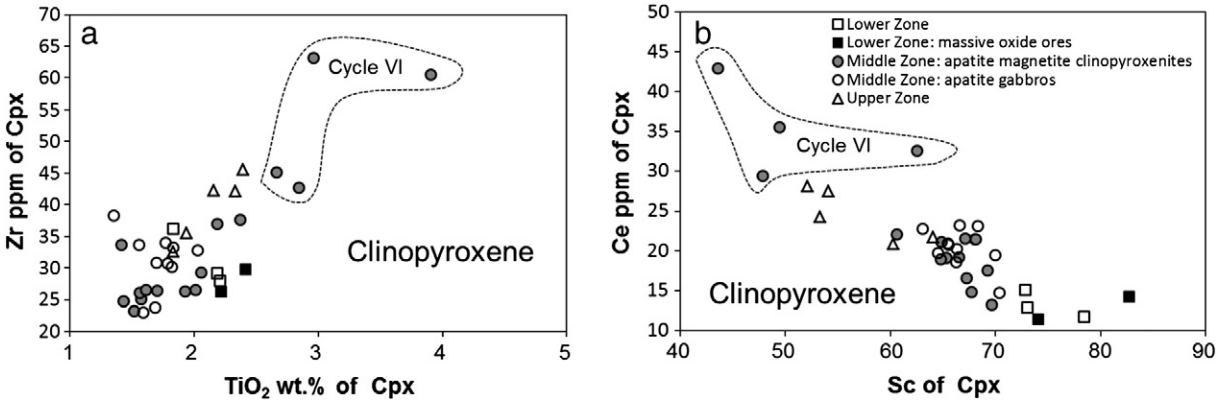

Fig. 11. (a) Binary plots of Zr vs TiO_2 of clinopyroxene; (b) binary plots of Ce vs Sc of clinopyroxene.

References

Ali, J.R., Thompson, G.M., Zhou, M.F., Song, X.Y., 2005. Emeishan large igneous province, SW China. Lithos 79, 475–489.

Bai, Z.J., Zhong, H., Naldrett, A.J., Zhu, W.G., Xu, G.W., 2012. Whole-rock and mineral composition constraints on the genesis of the giant Hongge Fe–Ti–V oxide deposit in the Emeishan large igneous province, southwest China. Econ. Geol. 107, 507–524.

Black, L.P., Kamo, S.L., Allen, C.M., Aleinikoff, J.N., Davis, D.W., Korsch, R.J., Foudoulis, C., 2003. TEMORA 1: a new zircon standard for Phanerozoic U–Pb geochronology. Chem. Geol. 200, 155–170.

Blundy, J., Wood, B., 2003. Partitioning of trace elements between crystals and melts. Earth Planet. Sci. Lett. 210, 383–397.

Cawthorn, R.C., Ashwal, I.D., 2009. Origin of anorthosite and magnetitite layers in the Bushveld Complex, constrained by major element compositions of plagioclase. J. Petrol. 50, 1607–1637.

Charlier, B., Grove, T.L., 2012. Experiments on liquid immiscibility along tholeiitic liquid lines of descent. Contrib. Mineral. Petrol. 164, 27–44.

Chung, S.L., Jahn, B., 1995. Plume–lithosphere interaction in generation of the Emeishan flood basalts at the Permian–Triassic boundary. Geology 23, 889–892.

Ganino, C., Arndt, N.T., Zhou, M.F., Gaillard, F., Chauvel, C., 2008. Interaction of magma with sedimentary wall rock and magnetite ore genesis in the Panzhihua mafic intrusion, SW China. Miner. Deposita 43, 677–694.

Gibson, S.A., Thompson, R.N., Dickin, A.P., 2000. Ferropicrites: geochemical evidence for Fe-rich streaks in upwelling mantle plumes. Earth Planet. Sci. Lett. 174, 355–374.

Green, T.H., Blundy, J.D., Adam, J., Yaxley, G.M., 2000. SIMS determination of trace element partition coefficients between garnet, clinopyroxene and hydrous basaltic liquids at 2–7.5 GPa and 1080–1200 °C. Lithos 53, 165–187.

Hanski, E.J., Smolkin, V.F., 1995. Iron- and LREE-enriched mantle source for early Proterozoic intraplate magmatism as exemplified by the Pechenga ferropicrites, Kola Peninsula, Russia. Lithos 34, 107–125.

Hart, S.R., Dunn, T., 1993. Experimental cpx/melt partitioning of 24 trace elements. Contrib. Mineral. Petrol. 113, 1–8.

Hauri, E.H., Wagner, T.P., Grove, T.L., 1994. Experimental and natural partitioning of Th, U, Pb and other trace elements between garnet, clinopyroxene and basaltic melts. Chem. Geol. 117, 149–166.

He, B., Xu, Y.G., Huang, X.L., Luo, Z.Y., Shi, Y.R., Yang, Q.J., Yu, S.Y., 2007. Age and duration of the Emeishan flood volcanism, SW China: geochemistry and SHRIMP zircon U–Pb dating of silicic ignimbrites, post-volcanic Xuanwei Formation and clay tuff at the Chaotian section. Earth Planet. Sci. Lett. 255, 306–323.

Hou, T., Zhang, Z.C., Kusky, T., Du, Y.S., Liu, J.L., Zhao, Z.D., 2011a. A reappraisal of the high-Ti and low-Ti classification of basalts and petrogenetic linkage between basalts and mafic–ultramafic intrusions in the Emeishan large igneous province, SW China. Ore Geol. Rev. 41, 133–143.

Hou, T., Zhang, Z.C., Ye, X.R., Encarnacion, J., Reichow, M.K., 2011b. Noble gas isotopic systematics of Fe–Ti–V oxide ore-related mafic–ultramafic layered intrusions in the

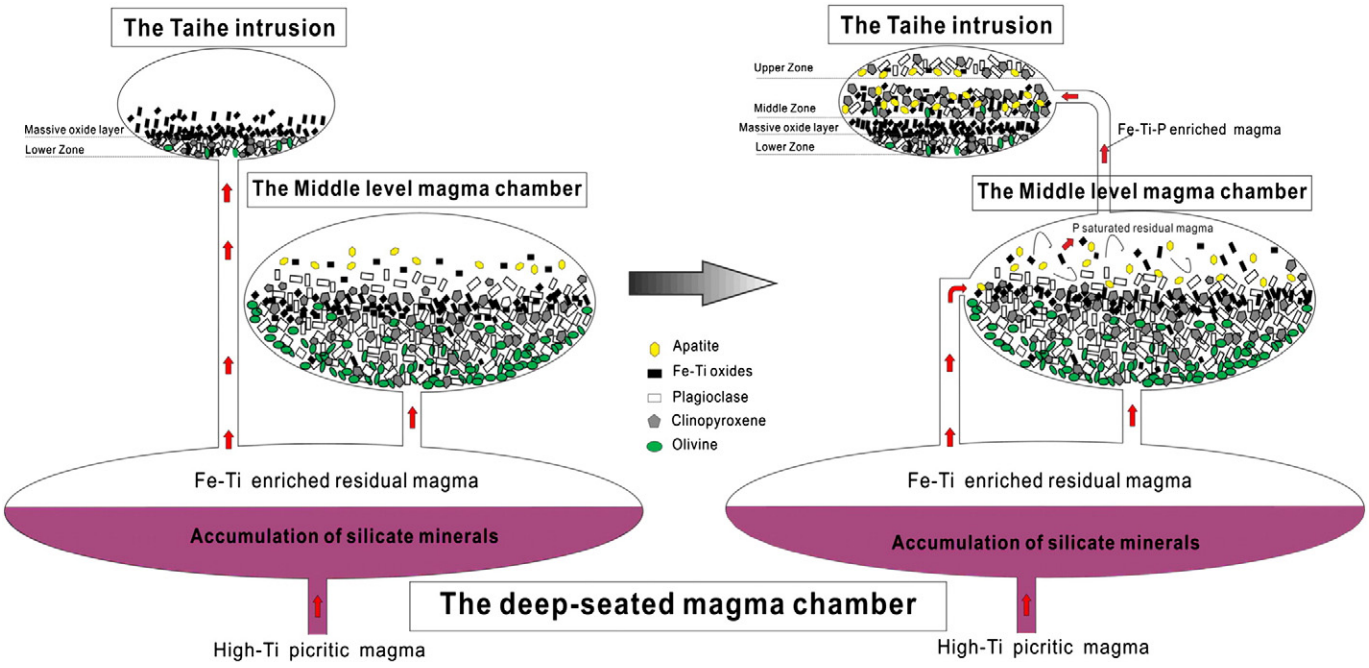

Fig. 12. The model of magma-plumbing system process of the Taihe intrusion.

Panxi area, China: the role of recycled oceanic crust in their petrogenesis. Geochim. Cosmochim. Acta 75, 6727–6741.
Hou, T., Zhang, Z.C., Encarnacion, J., Santosh, M., 2012a. Petrogenesis and metallogenesis of the Taihe gabbroic intrusion associated with Fe–Ti-oxide ores in the Panxi district, Emeishan Large Igneous Province, southwest China. Ore Geol. Rev. 49, 109–127.
Hou, T., Zhang, Z.C., Encarnacion, J., Santosh, M., Sun, Y.L., 2012b. The role recycled oceanic crust in magmatism and metallogenesis: Os–Sr–Nd isotpes, U–Pb geochronology and geochemistry of picritic dykes in the Panzhihua giant Fe–Ti oxide deposit, central Emeishan large igneous province. Contrib. Mineral. Petrol. 165, 805–822.
Kamenetsky, V.S., Chung, S.L., Kamenetsky, M.B., Kuzmin, D.V., 2012. Picrites from the Emeishan large igneous province, SW China: a compositional continuum in primitive magmas and their respective mantle sources. J. Petrol. 53, 2095–2113.
Klemme, S., Günther, D., Hametner, K., Prowatke, S., Zack, T., 2006. The partitioning of trace elements between ilmenite, ulvospinel, armalcolite and silicate melts with implications for the early differentiation of the moon. Chem. Geol. 234, 251–263.
Kolker, A., 1982. Mineralogy and geochemistry of Fe–Ti oxide and apatite (nelsonite) deposits and evaluation of the liquid immiscibility hypothesis. Econ. Geol. 77, 1146–1158.
Liu, Y.S., Hu, Z.C., Gao, S., Günther, D., Xu, J., Gao, C., Chen, H., 2008. In situ analysis of major and trace elements of anhydrous minerals by LA-ICP-MS without applying an internal standard. Chem. Geol. 257, 34–43.
Luan, Y., Song, X.-Y., Chen, L.-M., Zheng, W.-Q., Zhang, X.-Q., Yu, S.-Y., She, Y.-W., Tian, X.-L., Ran, Q.-Y., 2013. Key constrains on the formation of the Fe-Ti oxide accumulation in the Hongge layered intrusions in the Emeishan Large Igneous Province. SW China, Ore Geology Reviews 57, 518–538 (this issue).
Namur, O., Charlier, B., Toplis, M.J., Higgins, M.D., Liégeois, J.P., Vander Auwera, J., 2010. Crystallization sequence and magma chamber processes in the ferrobasaltic Sept Iles layered intrusion, Canada. J. Petrol. 51, 1203–1236.
Namur, O., Charlier, B., Holness, M.B., 2012. Dual origin of Fe–Ti–P gabbros by immiscibility and fractional crystallization of evolved tholeiitic basalts in the Sept Iles layered intrusion. Lithos 154, 100–114.
Nasdala, L., Hofmeister, W., Norberg, N., Martinson, J.M., Corfu, F., Dörr, W., Kamo, S.L., Kennedy, A.K., Kronz, A., Reiners, P.W., 2008. Zircon M257—a homogeneous natural reference material for the ion microprobe U–Pb analysis of zircon. Geostand. Geoanal. Res. 32, 247–265.
Naslund, H.R., 1983. The effect of oxygen fugacity on liquid immiscibility in iron-bearing silicate melts. Am. J. Sci. 283, 1034–1059.
Pang, K.N., Zhou, M.F., Lindsley, D., Zhao, D., Malpas, J., 2008. Origin of Fe–Ti oxide ores in mafic intrusions: evidence from the Panzhihua Intrusion, SW China. J. Petrol. 49, 295–313.
Pang, K.N., Zhou, M.F., Qi, L., Shellnutt, G., Wang, C.Y., Zhao, D.G., 2010. Flood basalt related Fe-Ti oxide deposits in the Emeishan large igneous province, SW China. Lithos 119, 123–136.
Panxi Geological Unit, 1984. Mineralization and Exploration Forecasting of V–Ti Magnetite Deposits in the Panzhihua–Xichang Region.
Philpotts, A.R., 1967. Origin of certain iron–titanium oxide and apatite rocks. Econ. Geol. 62, 303–315.
Philpotts, A.R., 1982. Compositions of immiscible liquids in volcanic rocks. Contrib. Mineral. Petrol. 80, 201–218.
Philpotts, A.R., Doyle, C.D., 1983. Effect of magma oxidation state on the extent of silicate liquid immiscibility in a tholeiitic basalt. Am. J. Sci. 283, 967–986.
Qi, L., Zhou, M.F., 2008. Platinum-group elemental and Sr–Nd–Os isotopic geochemistry of Permian Emeishan flood basalts in Guizhou Province, SW China. Chem. Geol. 248, 83–103.
Qi, L., Hu, J., D Conrad, G., 2000. Determination of trace elements in granites by inductively coupled plasma mass spectrometry. Talanta 51, 507–513.
Reynolds, I.M., 1985. The nature and origin of titaniferous magnetite-rich layers in the Upper Zone of the Bushveld Complex: a review and synthesis. Econ. Geol. 80, 1089–1108.
Roeder, P.L., Emslie, R.F., 1970. Olivine–liquid equilibrium. Contrib. Mineral. Petrol. 29, 275–289.
Shellnutt, J.G., Jahn, B.M., 2011. Origin of Late Permian Emeishan basaltic rocks from the Panxi region (SW China): implications for the Ti-classification and spatial–compositional distribution of the Emeishan flood basalts. J. Volcanol. Geotherm. Res. 199, 85–95.
Song, X.Y., Zhou, M.F., Hou, Z.Q., Cao, Z.M., Wang, Y.L., Li, Y., 2001. Geochemical constraints on the mantle source of the upper Permian Emeishan continental flood basalts, southwestern China. Int. Geol. Rev. 43, 213–225.
Song, X.Y., Zhou, M.F., Cao, Z.M., Robinson, P.T., 2004. Late Permian rifting of the South China Craton caused by the Emeishan mantle plume? J. Geol. Soc. Lond. 161, 773.
Song, X.Y., Qi, H.W., Robinson, P.T., Zhou, M.F., Cao, Z.M., Chen, L.M., 2008. Melting of the subcontinental lithospheric mantle by the Emeishan mantle plume; evidence from the basal alkaline basalts in Dongchuan, Yunnan, Southwestern China. Lithos 100, 93–111.
Song, X.Y., Keays, R.R., Xiao, L., Qi, H.W., Ihlenfeld, C., 2009. Platinum-group element geochemistry of the continental flood basalts in the central Emeisihan Large Igneous Province, SW China. Chem. Geol. 262, 246–261.
Song, X.Y., Qi, H.W., Hu, R.Z., Chen, L.M., Yu, S.Y., Zhang, J.F., 2013. Formation of thick stratiform Fe-Ti oxide layers in layered intrusion and frequent replenishment of fractionated mafic magma: evidence from the Panzhihua intrusion, SW China. Geochem. Geophys. Geosyst. 14, 712–732.
Sun, S.S., McDonough, W.F., 1989. Chemical and isotopic systematics of oceanic basalts: implications for mantle composition and processes. In: Saunders, A.D., Norry, M.J. (Eds.), Magmatism in the Ocean BasinGeol. Soc. Lond. Spec. Publ, 42, pp. 313–345.
Tegner, C., Cawthorn, R.G., Kruger, F.J., 2006. Cyclicity in the Main and Upper Zones of the Bushveld Complex, South Africa: crystallization from a zoned magma sheet. J. Petrol. 47, 2257–2279.
Tollari, N., Toplis, M.J., Barnes, S.J., 2006. Predicting phosphate saturation in silicate magmas: an experimental study of the effects of melt composition and temperature. Geochim. Cosmochim. Acta 70, 1518–1536.
Tollari, N., Barnes, S.J., Cox, R.A., Nabil, H., 2008. Trace element concentrations in apatites from the Sept-Îles Intrusive Suite, Canada—implications for the genesis of nelsonites. Chem. Geol. 252, 180–190.
Toplis, M.J., Carroll, M.R., 1995. An experimental study of the influence of oxygen fugacity on Fe–Ti oxide stability, phase relations, and mineral–melt equilibria in ferro-basaltic systems. J. Petrol. 36, 1137–1170.
Toplis, M.J., Libourel, G., Carroll, M.R., 1994. The role of phosphorus in crystallisation processes of basalt: an experimental study. Geochim. Cosmochim. Acta 58, 797–810.

VanTongeren, J.A., Mathez, E.A., 2012. Large-scale liquid immiscibility at the top of the Bushveld Complex, South Africa. Geology 20, 491–494.
Veksler, I., Dorfman, A., Danyushevsky, L., Jakobsen, J., Dingwell, D., 2006. Immiscible silicate liquid partition coefficients: implications for crystal-melt element partitioning and basalt petrogenesis. Contrib. Mineral. Petrol. 152, 685–702.
Wager, L.R., Brown, G.M., 1968. Layered Igneous Rocks.Oliver and Boyd, Edinburgh and London.
Wang, C.Y., Zhou, M.F., Qi, L., 2007. Permian flood basalts and mafic intrusions in the Jinping (SW China)–Song Da (northern Vietnam) district: mantle sources, crustal contamination and sulfide segregation. Chem. Geol. 243, 317–343.
Xiao, L., Xu, Y.G., Mei, H.J., Zheng, Y.F., He, B., Pirajno, F., 2004. Distinct mantle sources of low-Ti and high-Ti basalts from the western Emeishan large igneous province, SW China: implications for plume–lithosphere interaction. Earth Planet. Sci. Lett. 228, 525–546.
Xu, Y.G., Chung, S.L., Jahn, B.M., Wu, G., 2001. Petrologic and geochemical constraints on the petrogenesis of Permian–Triassic Emeishan flood basalts in southwestern China. Lithos 58, 145–168.
Xu, Y.G., Luo, Z.Y., Huang, X.L., He, B., Xiao, L., Xie, L.W., Shi, Y.R., 2008. Zircon U–Pb and Hf isotope constraints on crustal melting associated with the Emeishan mantle plume. Geochim. Cosmochim. Acta 72, 3084–3104.
Zhang, Z.C., Mahoney, J.J., Mao, J.W., Wang, F.S., 2006. Geochemistry of picritic and associated basalt flows of the western Emeishan flood basalt province, China. J. Petrol. 47, 1997–2019.
Zhang, Z.C., Mao, J.W., Saunders, A.D., Ai, Y., Li, Y., Zhao, L., 2009. Petrogenetic modeling of three mafic–ultramafic layered intrusions in the Emeishan large igneous province, SW China, based on isotopic and bulk chemical constraints. Lithos 113, 369–392.
Zhang, X.Q., Song, X.Y., Chen, L.M., Xie, W., Yu, S.Y., Zheng, W.Q., Deng, Y.F., Zhang, J.F., Gui, S.G., 2012. Fractional crystallization and the formation of thick Fe–Ti–V oxide layers in the Baima layered intrusion, SW China. Ore Geol. Rev. 49, 96–108.
Zhong, H., Zhu, W.G., 2006. Geochronology of layered mafic intrusions from the Pan-Xi area in the Emeishan large igneous province, SW China. Miner. Deposita 41, 599–606.
Zhong, H., Zhou, X.H., Zhou, M.F., Sun, M., Liu, B.G., 2002. Platinum-group element geochemistry of the Hongge Fe–V–Ti deposit in the Pan-Xi area, southwestern China. Miner. Deposita 37, 226–239.
Zhong, H., Campbell, I.H., Zhu, W.G., Allen, C.M., Hu, R.Z., Xie, L.W., He, D.F., 2011. Timing and source constraints on the relationship between mafic and felsic intrusions in the Emeishan large igneous province. Geochim. Cosmochim. Acta 75, 1374–1395.
Zhou, M.F., Malpas, J., Song, X.Y., Robinson, P.T., Sun, M., Kennedy, A.K., Lesher, C.M., Keays, R.R., 2002. A temporal link between the Emeishan large igneous province (SW China) and the end-Guadalupian mass extinction. Earth Planet. Sci. Lett. 196, 113–122.
Zhou, M.F., Robinson, P.T., Lesher, C.M., Keays, R.R., Zhang, C.J., Malpas, J., 2005. Geochemistry, petrogenesis and metallogenesis of the Panzhihua gabbroic layered intrusion and associated Fe–Ti–V oxide deposits, Sichuan Province, SW China. J. Petrol. 46, 2253–2280.
Zhou, M.F., Zhao, J.H., Qi, L., Su, W.C., Hu, R.Z., 2006. Zircon U–Pb geochronology and elemental and Sr–Nd isotope geochemistry of Permian mafic rocks in the Funing area, SW China. Contrib. Mineral. Petrol. 151, 1–19.
Zhou, M.F., Arndt, N.T., Malpas, J., Wang, C.Y., Kennedy, A.K., 2008. Two magma series and associated ore deposit types in the Permian Emeishan large igneous province, SW China. Lithos 103, 352–368.